Interpreting azimuthal Fourier coefficients for anisotropic and fracture parameters

Jonathan E. Downton[1] and Benjamin Roure[2]

Abstract

Amplitude variation with offset and azimuth (AVOAz) analysis can be separated into two separate parts: amplitude variation with offset (AVO) analysis and amplitude versus azimuth (AVAz) analysis. Useful information about fractures and anisotropy can be obtained just by examining the AVAz. The AVAz can be described as a sum of sinusoids of different periodicities, each characterized by its magnitude and phase. This sum is mathematically equivalent to a Fourier series, and hence the coefficients describing the AVAz response are azimuthal Fourier coefficients (FCs). This FC parameterization is purely descriptive. The aim of this paper is to help the interpreter understand what these coefficients mean in terms of anisotropic and fracture parameters for the case of P-wave reflectivity using a linearized approximation. The FC representation is valid for general anisotropy. However, to gain insight into the significance of FCs, more restrictive assumptions about the anisotropy or facture system must be assumed. In the case of transverse anisotropic media with a horizontal axis of symmetry, the P-wave reflectivity linearized approximation may be rewritten in terms of azimuthal FCs with the magnitude and phase of the different FCs corresponding to traditional AVAz attributes. Linear slip theory is used to show that the FCs can be interpreted similarly for the cases of a single set of parallel vertical fractures in isotropic media and in transverse anisotropic media with a vertical axis of symmetry (VTI). The magnitude of the FCs depends on the fracture weakness parameters and the background media. For the case of vertical fractures in a VTI background, the AVOAz inverse problem is underdetermined, so extra information must be incorporated to determine how the weights are modified due to this background anisotropy. We evaluated this on a 3D data set from northwest Louisiana for which the main target was the Haynesville shale.

Introduction

P-wave amplitude variation with offset (AVO), or amplitude versus angle (AVA) as it should more correctly be known, has proven to be an important technology to characterize reservoirs in isotropic media, especially with the use of the Aki-Richards linearized approximation (Aki and Richards, 1980). This equation can also be readily extended to transverse anisotropic media with a vertical symmetry axis (VTI) such as shales (Thomsen, 1993; Rüger, 2002). As we will show in the next section, isotropic and VTI cases are a function of the incident, or polar, angle alone. Thus, VTI behavior in AVO is difficult to distinguish from isotropic behavior. In fractured media, it has proven beneficial to examine amplitude variation with offset and azimuth (AVOAz) response (Gray and Todorovic-Marinic, 2004; Xia et al., 2007). This now introduces a second angle, the azimuthal angle, which gives us two angles with which to extract anisotropic parameters, making the evaluation of azimuthal anisotropy less nonunique than the evaluation of VTI, or polar, anisotropy. (This assumes, of course, that you have a good range of observed azimuths.) The presence of fractures introduces anisotropy (Schoenberg, 1980; Hudson, 1981), necessitating the use of a more complex reflectivity expression. Thomsen (1993), Rüger (1998), and Pšenčik and Martins (2001) derive P-wave-linearized AVOAz relationships for anisotropic media of differing complexity. Analyzing and fitting data using these AVOAz relationships is more difficult than with AVO analysis because of the extra dimensionality of the problem. One way to simplify the analysis is to split the problem into two parts: amplitude versus azimuth (AVAz) and AVO analyses.

The AVAz response can be written in terms of a Fourier series (Ikelle, 1996; Sayers and Dean, 2001). Note that a Fourier series is a sum of weighted sinusoids of differing periodicities. The weights describing the sinusoids are called Fourier coefficients (FCs), which are dependent on the angle of incidence. By analyzing data from one particular incidence angle, it is possible to analyze just the AVAz reflectivity. The azimuthal FCs describing the AVAz behavior are estimated using a

[1]CGG GeoSoftware, Calgary, Alberta, Canada. E-mail: jon.downton@cgg.com.
[2]CGG GeoConsulting, Calgary, Alberta, Canada. E-mail: benjamin.roure@cgg.com.
Manuscript received by the Editor 15 October 2014; revised manuscript received 13 February 2015; published online 26 May 2015. This paper appears in *Interpretation*, Vol. 3, No. 3 (August 2015); p. ST9–ST27, 13 FIGS., 4 TABLES.
http://dx.doi.org/10.1190/INT-2014-0235.1.

Fourier transform. Because of the orthogonality of the Fourier transform, each of these azimuthal FCs conveys unique and independent information about the azimuthal data, making them ideal attributes to interpret. One of the key benefits of using these azimuthal FCs is that they are descriptive in nature. It is possible to look at the AVAz response and have an intuitive feel for what the azimuthal FCs should be and whether the calculated values are reasonable.

We begin by reviewing AVO in isotropic and VTI media. The AVOAz reflectivity (Rüger, 1998) for transverse anisotropic media with a horizontal symmetry axis (HTI) is then separated into its constituent parts. The AVO part has the same form as the isotropic case. The AVAz part is written in terms of a Fourier series. The magnitude of the second FC is proportional to the anisotropic gradient, whereas the magnitude of the fourth FC is a function of the anellipticity. These concepts are illustrated with a simple example. Next, the calculation of the azimuthal FCs is discussed along with some practical considerations in performing these calculations on real data.

The case of general anisotropy is studied by rearranging the Pšenčik and Martins (2001) linearized PP reflectivity expression as a Fourier series. This has the same basic form as the HTI formulation but with differing FCs. The FCs are functions of a total of nine parameters that, in turn, are functions of the stiffness coefficients and density. The case of general anisotropy has 21 stiffness coefficients, and hence the P-wave AVOAz inverse problem for the general anisotropy is nonunique (Pšenčik and Martins, 2001). This is true for any symmetry requiring eight parameters or more to describe it, such as orthorhombic or monoclinic anisotropy. Note that the anisotropy due to a conjugate set of fractures is generally monoclinic or in the case of dipping fractures triclinic. The number of parameters can be reduced by assuming some rock physics model. Linear slip (LS) theory (Schoenberg, 1980; Schoenberg and Douma, 1988; Schoenberg and Helbig, 1997) is used to calculate the azimuthal FCs for the case of a set of parallel vertical fractures in an isotropic (VFI) background rock. The anisotropy due to VFI is generally orthorhombic, but for the subcase of rotationally symmetric fractures, the anisotropy is HTI. In this special case, the azimuthal FCs reduce to that of Downton et al. (2011) and can be directly compared to the HTI (Rüger, 1998) reflectivity expressions. By comparing these two formulations, it is evident that the anisotropic gradient can be estimated using only FCs calculated from the AVAz data.

Many shale gas reservoirs are thought to be VTI, so the case of vertical fractures in a transverse isotropic (VFTI) background rock is studied last. The presence of VTI anisotropy modifies the expressions of the azimuthal FCs. Similar to VTI AVO, the VFTI AVOAz inverse problem is underdetermined. However, if some knowledge of the background anisotropy exists, it is possible to predict how the VFTI AVOAz response differs from the VFI base case. This is illustrated using a 3D data set from northwest Louisiana for which the main target is the Haynesville Formation. This data set is first used to compare anisotropic gradient estimates calculated using FCs and AVOAz inversion. Then, a modeling study is performed to try and understand the influence of the background VTI anisotropy on the azimuthal FCs.

Amplitude variation with offset

To study the AVOAz response, it is instructive to separate the amplitude response into its constituent AVO and AVAz parts. The linearized AVO or more precisely the AVA P-wave reflectivity in isotropic (Aki and Richards, 1980; Swan, 1993) and VTI media (Thomsen, 1993; Blangy, 1994; Rüger, 2002) is given by

$$R(\theta) = A + B\sin^2\theta + C\sin^2\theta\tan^2\theta \tag{1}$$

and is solely a function of the angle of incidence θ. The intercept A, gradient B, and curvature C are linear combinations of the fractional material contrasts across a simple interface. In isotropic media, these are defined as

$$A = \frac{\Delta V_P}{2\bar{V}_P} + \frac{\Delta\rho}{2\bar{\rho}}, \tag{2}$$

$$B_{iso} = \frac{\Delta V_P}{2\bar{V}_P} - 4\frac{\bar{V}_S^2}{\bar{V}_P^2}\left[\frac{\Delta V_S}{\bar{V}_S} + \frac{\Delta\rho}{2\bar{\rho}}\right], \tag{3}$$

and

$$C_{iso} = \frac{\Delta V_P}{2\bar{V}_P}, \tag{4}$$

where ρ, V_P, and V_S are the density and the P- and S-wave velocities. The symbol Δ denotes a difference, whereas an overbar represents the average of the material properties across the interface. In VTI media, the B and C parameters

$$B_{VTI} = B_{iso} + \frac{\Delta\delta}{2} \tag{5}$$

and

$$C_{VTI} = C_{iso} + \frac{\Delta\varepsilon}{2} \tag{6}$$

are perturbed by $\Delta\varepsilon$ and $\Delta\delta$. The fractional Thomsen (1986) parameters ε, δ, and γ describe the degree of anisotropy relative to the vertical P- and S-wave velocities within the media. The vertical P- and S-wave veloc-

ities defined in terms of stiffness coefficients are $V_P = \sqrt{c_{33}/\rho}$ and $V_S = \sqrt{c_{44}/\rho}$.

The AVO reflectivity is a weighted sum of the intercept, gradient, and curvature. Given data at three or more unique angles, it is possible to estimate parameters A, B, and C. If the media are known to be isotropic, it is then possible to estimate the density, P-wave velocity, and S-wave velocity (Buland and Omre, 2003). However, if the media are VTI, then there are two additional unknown parameters and the inversion to material properties is underdetermined. In practice, due to limitations of the data acquisition and noise, the near-offset AVO approximation

$$R(\theta) = A + B\sin^2\theta \tag{7}$$

is often inverted providing estimates of only two parameters.

Equations 1 and 7 exhibit no azimuthal dependence. If the seismic amplitude data also vary as a function of azimuth, this extra information may be used to infer additional parameters about the earth's material properties.

Amplitude variation with offset and azimuth for transverse anisotropic media with a horizontal symmetry axis

In HTI media, the amplitude also varies as a function of azimuth. The linearized P-wave reflectivity at the interface between two HTI media that share the same symmetry axis ϕ_{sym} as a function of polar angle θ and azimuth ϕ is (Rüger, 1998)

$$\begin{aligned} R(\phi,\theta) = &\frac{\Delta Z}{2\overline{Z}} + \frac{1}{2}\left(\left[\frac{\Delta V_P}{\overline{V}_P} - \left(2\frac{\overline{V}_S}{\overline{V}_P}\right)^2\frac{\Delta G}{\overline{G}}\right]\right. \\ &+ \left[\Delta\delta^{(v)} + 8\left(\frac{\overline{V}_S}{\overline{V}_P}\right)^2\Delta\gamma\right]\cos^2(\phi-\phi_{sym})\Big)\sin^2\theta \\ &+ \left(\frac{\Delta V_P}{2\overline{V}_P} + \frac{1}{2}(\Delta\varepsilon^{(v)}\sin^2(\phi-\phi_{sym})\right. \\ &\left.+ \Delta\delta^{(v)}\cos^2(\phi-\phi_{sym}))\sin^2(\phi-\phi_{sym})\right)\sin^2\theta\tan^2\theta, \end{aligned} \tag{8}$$

where $Z = \rho V_P$ is the vertical P-wave impedance and $G = c_{44} = \rho V_S^2$ is the shear modulus. The superscript v on the fractional Thomsen (1986) parameters indicate that $\varepsilon^{(v)}$ and $\delta^{(v)}$ are referenced to the vertical axis rather than the symmetry axis. Table 1 in Rüger (1998) describes the transformations between the two parameterizations. Equation 8 is sometimes written in terms of $\gamma^{(v)}$ as

$$\begin{aligned} R(\phi,\theta) = &\frac{\Delta Z}{2\overline{Z}} + \frac{1}{2}\left(\left[\frac{\Delta V_P}{\overline{V}_P} - \left(2\frac{\overline{V}_S}{\overline{V}_P}\right)^2\frac{\Delta G}{\overline{G}}\right]\right. \\ &+ \left[\Delta\delta^{(v)} - 8\left(\frac{\overline{V}_S}{\overline{V}_P}\right)^2\Delta\gamma^{(v)}\right]\cos^2(\phi-\phi_{sym})\Big)\sin^2\theta \\ &+ \left(\frac{\Delta V_P}{2\overline{V}_P} + \frac{1}{2}(\Delta\varepsilon^{(v)}\sin^2(\phi-\phi_{sym})\right. \\ &\left.+ \Delta\delta^{(v)}\cos^2(\phi-\phi_{sym}))\sin^2(\phi-\phi_{sym})\right)\sin^2\theta\tan^2\theta, \end{aligned} \tag{9}$$

making use of the linearized approximation $\gamma \approx -\gamma^{(v)}$, but at a loss of accuracy (Rüger, 2002). This second version can be rewritten in terms of the fracture weakness parameters without further approximations and so is used in this paper.

Typically, for real seismic data, the near-offset approximation

$$R(\phi,\theta) = A + (B_{iso} + B_{ani}\cos^2(\phi-\phi_{sym}))\sin^2\theta \tag{10}$$

is used to infer the parameters from the AVOAz data. Equation 10 is parameterized in a similar fashion as the isotropic AVA equation using

$$\begin{aligned} B_{iso} &= \frac{1}{2}\left[\frac{\Delta V_P}{\overline{V}_P} - \left(2\frac{\overline{V}_S}{\overline{V}_P}\right)^2\frac{\Delta G}{\overline{G}}\right] \\ &= \frac{\Delta V_P}{2\overline{V}_P} - 4\frac{\overline{V}_S^2}{\overline{V}_P^2}\left[\frac{\Delta V_S}{\overline{V}_S} + \frac{\Delta\rho}{2\overline{\rho}}\right] \end{aligned} \tag{11}$$

and

$$B_{ani} = \frac{1}{2}\left[\Delta\delta^{(v)} - 8\left(\frac{\overline{V}_S}{\overline{V}_P}\right)^2\Delta\gamma^{(v)}\right]. \tag{12}$$

Compared to two-term AVO inversion, the near-offset Rüger approximation provides the interpreter with two additional parameter estimates: the anisotropic gradient B_{ani} and the symmetry axis azimuth ϕ_{sym}. A nonzero anisotropic gradient implies that the media is anisotropic. The exact interpretation is complicated by the fact that B_{ani} is a weighted difference of the Thomsen parameters $\delta^{(v)}$ and $\gamma^{(v)}$, and it is possible for the two to cancel out. In the "Single set of vertical fractures in isotropic background media" section it is shown that the anisotropic gradient is a function of fracture weakness parameters and that, for a single vertical fracture, the isotropy plane azimuth is parallel to the fracture strike. The isotropy plane azimuth is perpendicular to the symmetry axis azimuth.

Further complicating the interpretation is that the solution for B_{ani} and ϕ_{sym} is nonunique. The nonlinear inversion of equation 10 results in two solutions that fit the data equally well. Estimating B_{ani} involves taking the square root of an intermediate result (Downton and Gray, 2006), thus introducing a sign ambiguity. Choosing the wrong sign for B_{ani} introduces a 90° shift to the estimate of ϕ_{sym} and biases B_{iso}.

Figure 1 shows a synthetic gather generated using equation 8 based on the parameters in Tables 1 and 2. The amplitude varies as a function of azimuth and angle of incidence. These changes are more apparent if the amplitude data are displayed as a polar plot (Figure 2a). It is not obvious from equation 8 how a particular parameter impacts the AVOAz. Figure 2b and 2c shows the separate AVA and AVAz responses. The AVAz response is sinusoidal, with the magnitude of the sinusoids increasing as a function of angle of incidence. The next section, "Amplitude variation with azimuth for transverse anisotropic media with a horizontal symmetry axis," shows that by rewriting the P-wave reflectivity solely as a function of azimuth, it becomes more obvious how the different parameters impact the amplitude.

Amplitude variation with azimuth for transverse anisotropic media with a horizontal symmetry axis

To understand the AVAz response, the HTI Rüger equation 9 is rewritten in the form of the Fourier series

Table 1. Parameters used to generate the anelliptic model.

Layer	V_P (m/s)	V_S (m/s)	ρ (kg/m^3)	$\varepsilon^{(v)}$	$\delta^{(v)}$	γ
1	3800	1900	2450	0	0	0
2	4152	2100	2550	−0.0349	−0.1157	0.125

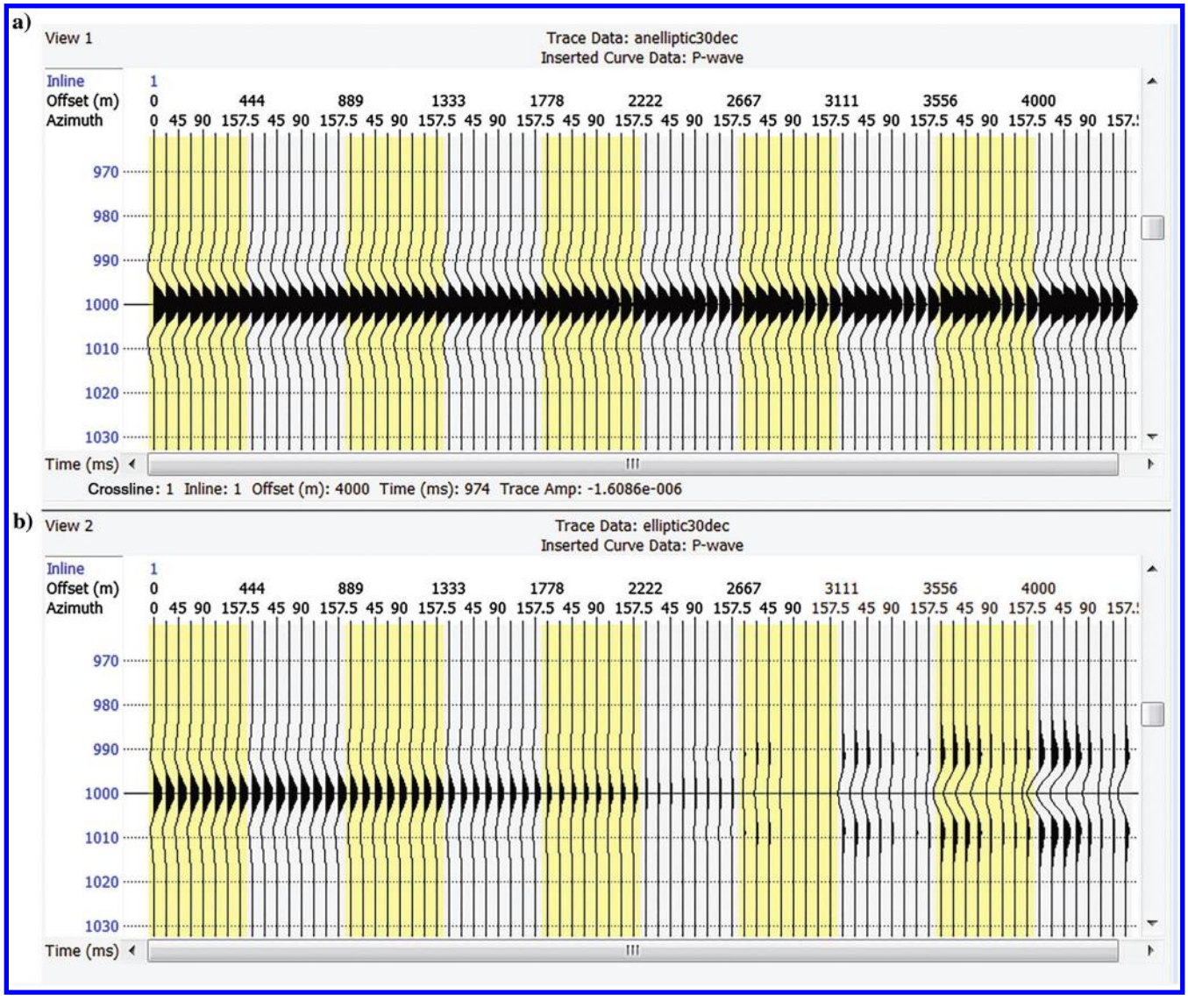

Figure 1. Synthetic gathers generated using the HTI Rüger equation 8 based on elastic models listed in Tables 1 and 2. Synthetic gather (a) is generated with anelliptical anisotropy, whereas synthetic gather (b) is generated with elliptical anisotropy. Both have the same S-wave anisotropy. To emphasize the azimuthal variations within the common offsets, the data are displayed with an alternating yellow and gray background that corresponds to the common offset panels.

$$R(\phi,\theta) = r_0(\theta) + \sum_{n=1}^{\infty} r_n(\theta)\cos(n(\phi - \phi_n(\theta))). \quad (13)$$

The FCs describing each sinusoid are the magnitude $r_n(\theta)$ and the phase $\phi_n(\theta)$, both varying as a function of the incidence angle. The azimuthal reflectivity at a particular angle of incidence θ is the superposition of a series of sinusoids weighted by factor r_n of period n and phase delayed by phase terms ϕ_n. Only the $n = 0$, 2, and 4 magnitude weighting terms are nonzero, and thus equation 13 simplifies to

$$R(\phi,\theta) = r_0(\theta) + r_2(\theta)\cos(2(\phi - \phi_2(\theta))) + r_4(\theta)\cos(4(\phi - \phi_4(\theta))), \quad (14)$$

with magnitudes

$$r_0(\theta) = A_0 + B_0\sin^2\theta + C_0\sin^2\theta\tan^2\theta, \quad (15)$$

Table 2. Parameters used to generate the elliptical model.

Layer	V_P (m/s)	V_S (m/s)	ρ (kg/m^3)	$\varepsilon^{(v)}$	$\delta^{(v)}$	γ
1	3800	1900	2450	0	0	0
2	3929	2100	2550	−0.2143	−0.2143	0.125

$$r_2(\theta) = \frac{1}{2}B_{\text{ani}}\sin^2\theta + \frac{\Delta\varepsilon^{(v)}}{4}\sin^2\theta\tan^2\theta, \quad (16)$$

$$r_4(\theta) = \frac{\Delta\eta^{(v)}}{16}\sin^2\theta\tan^2\theta, \quad (17)$$

and phase $\phi_n(\theta) = \phi_{\text{sym}}$.

The HTI P-wave AVAz reflectivity is simply the sum of three sinusoids of periodicity $n = 0$, 2, and 4, whose magnitudes are governed by equations 15–17 and phase-delayed ϕ_{sym}. Figure 3 shows the appropriately weighted sinusoids calculated for the azimuthal data for the incidence angle centered at 40° from Figure 2. The zeroth-order FC magnitude (equation 15) introduces a bias based on the AVO trend and has the same form as the isotropic AVO equation 1. The parameters A_0, B_0, and C_0 given by

$$A_0 = A_{\text{iso}}, \quad B_0 = B_{\text{iso}} + \frac{1}{2}B_{\text{ani}}, \quad \text{and } C_0 = C_{\text{iso}} + \frac{3}{16}\Delta\varepsilon^{(V)} - \frac{1}{16}\Delta\delta^{(V)} \quad (18)$$

are modified from the isotropic case (equations 2–4) by the presence of the anisotropy.

The parameter $\eta^{(v)}$ (Tsvankin, 2001), defined as

$$\eta^{(v)} = \frac{\varepsilon^{(v)} - \delta^{(v)}}{1 + 2\delta^{(v)}}, \quad (19)$$

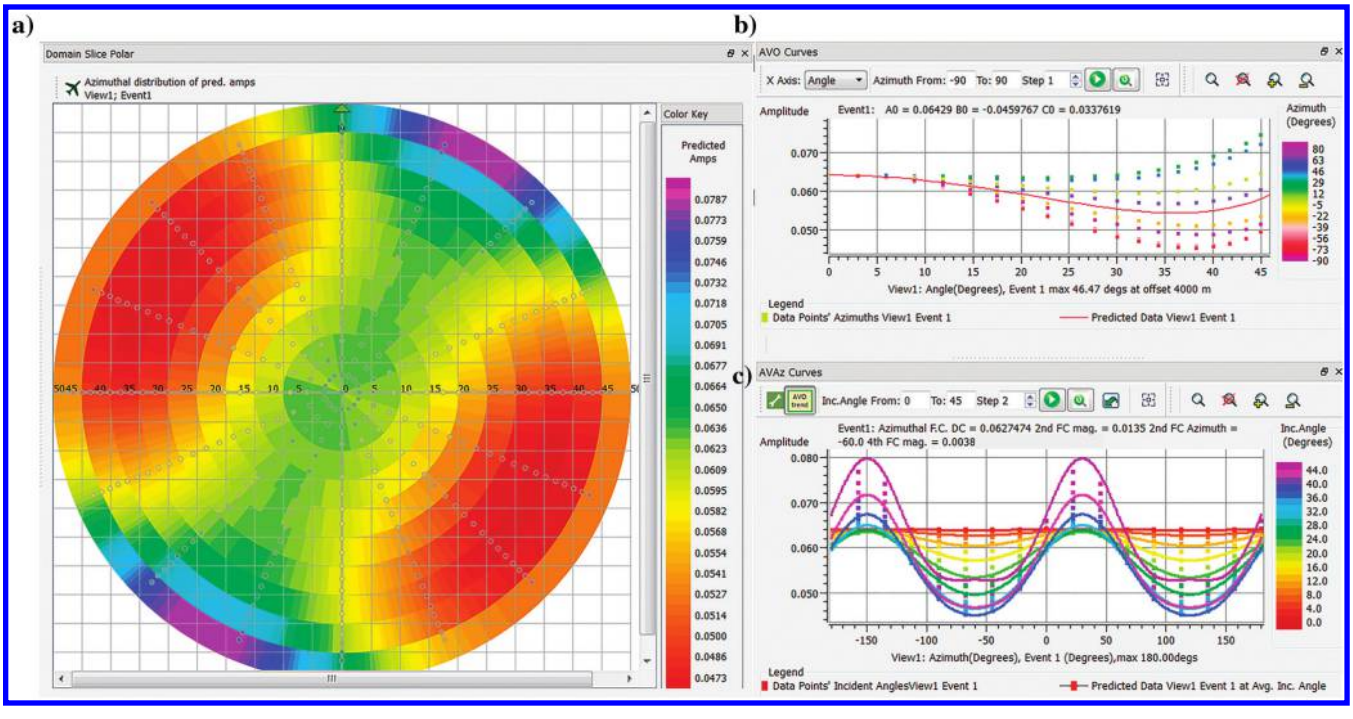

Figure 2. (a) The amplitude versus angle of incidence and azimuth, (b) AVA, and (c) AVAz of a synthetic gather generated using the Rüger equation 8 based on the parameters in Table 1. In the AVA display (b), the data points are color coded by azimuth. Note that the amplitude systematically varies about the average AVA trend line. The sinusoidal AVAz response (c) is displayed with the incidence angle displayed in color.

describes the anellipticity. The $n = 4$ magnitude (equation 17) is controlled by the change in anellipticity $\eta^{(v)}$ between layers. The magnitude of the fourth FC increases as a function of $\sin^2\theta\tan^2\theta$ and becomes significant at larger angles. This is illustrated in Figure 3. The model used to generate the AVAz response is anelliptic and has a nonzero fourth FC magnitude. Figure 4 contrasts this to the AVAz response generated for a model with an elliptical anisotropy (Table 2). Rasolofosaon (1998) and Gurevich et al. (2011) suggest that stress-induced anisotropy is elliptical. Because the anisotropy due to VFI background media is generally anelliptic (Bakulin et al., 2000), inverting for $\eta^{(v)}$ could help determine the source of the anisotropy.

The magnitude of the second FC (equation 16) is a weighted sum of B_{ani} and $\Delta\varepsilon^{(v)}$. The weights are angle dependent, and at near angles, the $\sin^2\theta$ term dominates the $\sin^2\theta\tan^2\theta$ term; thus, the magnitude of the second FC may be approximated as

$$r_2(\theta) \approx \frac{1}{2}B_{\text{ani}}\sin^2\theta. \tag{20}$$

This approximation provides an alternative method to estimate B_{ani} instead of inverting equation 9 or 10.

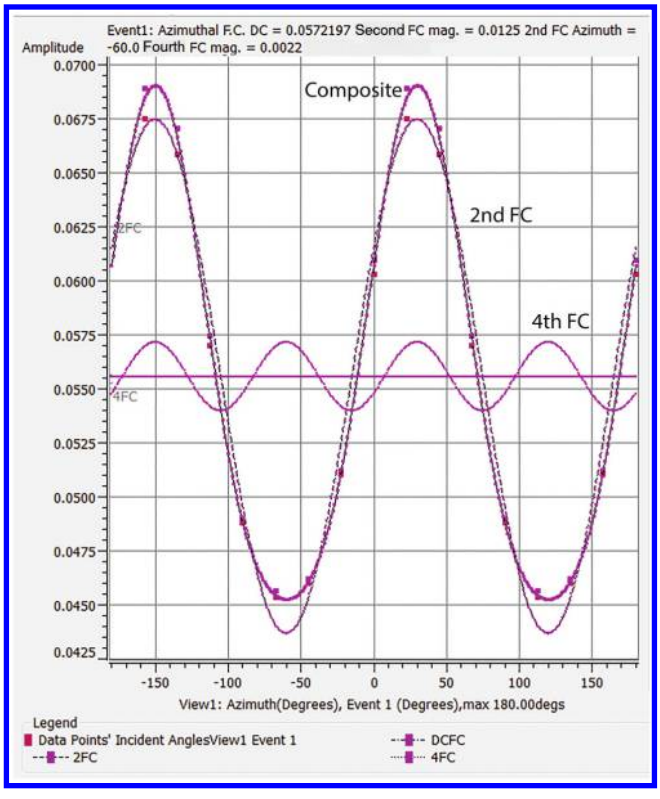

Figure 3. AVAz for the data from Figure 2 centered at an angle of incidence of 40°. The three sinusoids calculated from the Fourier analysis are shown as well as the total response. The $n = 0$ sinusoid (or DC) shifts the total response up or down. The second and fourth FCs control the azimuthal response. Note that the $n = 2$ and $n = 4$ sinusoids are phase shifted by 30°, which corresponds to ϕ_{sym}. For display purposes, the second and fourth sinusoids are shifted by the DC.

The parameter B_{ani} is simply estimated by observing the amplitude of the $n = 2$ sinusoid at some incidence angle (i.e., substitute $r_2(\theta)$ into equation 20 and solve for B_{ani}). The phase of the sinusoid is used to estimate the symmetry axis azimuth ϕ_{sym}.

Calculation of azimuthal Fourier coefficients

In the previous section, the Fourier series was written in terms of magnitude and phase. In calculating the FCs, it is more convenient to write the Fourier series as the weighted sum of cosine and sine waves

$$R(\phi,\theta) = \sum_{n=0}^{\infty}(u_n(\theta)\cos(n\phi) + v_n(\theta)\sin(n\phi)). \tag{21}$$

For the case of N regularly sampled data, the cosine coefficients u_n are calculated using

$$u_n(\theta) = \frac{1}{\pi}\sum_{k=1}^{N}R_k(\phi,\theta)\cos(n\phi)d\phi, \tag{22}$$

whereas the sine coefficients v_n are calculated using

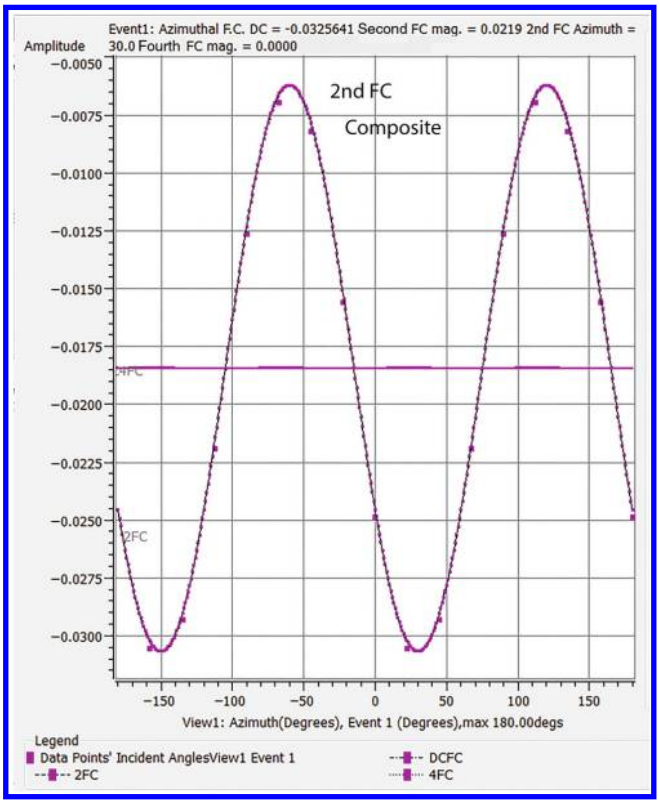

Figure 4. The AVAz centered at an angle of incidence of 40° for the synthetic generated from Table 2. The three sinusoids calculated from the Fourier analysis are shown as well as the total response. The fourth FC's magnitude is zero in this case because of the elliptical anisotropy; thus, the total AVAz response is controlled by $n = 2$ FCs. For display purposes the second and fourth sinusoids are shifted by the DC.

$$v_n(\theta) = \frac{1}{\pi}\sum_{k=1}^{N} R_k(\phi,\theta)\sin(n\phi)d\phi \tag{23}$$

for integer values of n such that $n \geq 0$. These parameters can be transformed to magnitude

$$r_n(\theta) = \sqrt{u_n^2(\theta) + v_n^2(\theta)}, \tag{24}$$

and phase

$$\phi_n(\theta) = \frac{1}{n}\arctan\left(\frac{v_n(\theta)}{u_n(\theta)}\right). \tag{25}$$

In practice, the workflow for calculating the FCs depends on the geometry of the data. The simplest case is for regularly sampled data in the azimuth, such as the output of an azimuthally sectored migration. If necessary, the seismic data are transformed from offset to angle of incidence for each azimuth sector. Then, the data are grouped by angle of incidence. For each incidence angle, equations 22 and 23 are used to calculate the angle-dependent azimuthal FCs. The magnitude and phase can, in turn, be calculated using equations 24 and 25. This is done for each common depth point location and time sample.

The data migrated using a common offset vector (COV) (Cary, 1999; Vermeer, 2002) approach are irregularly sampled in the azimuth and offset domains. For the case of irregularly sampled data, least-squares inversion of equation 21 can be performed to obtain the FCs. To accurately estimate each sinusoid, there should be at least four data points per period. This sometimes can be challenging for the $n = 4$ FC, particularly for azimuthally migrated data. For COV-migrated data, the azimuthal sampling increases as a function of offset, so typically, the sampling is adequate to estimate the fourth FC. To build up sufficient fold to perform this inversion in a stable fashion, the data must be binned over some angle range, centered on the angle for which the analysis is to be performed. This binning introduces smearing, which adversely impacts the analysis. This can be mitigated by performing some form of bin-centering operation.

The estimate of the azimuth is complicated by phase wrapping. Phase wrapping occurs due to the periodicity of the sine and cosine functions. It gets worse as n gets larger. The possible range of the arctan function in equation 25 is 180°. If $n = 2$, the possible range is reduced to 90°, and for $n = 4$, the possible range is only 45°. This complicates the interpretation of the phase of the fourth FC.

Amplitude variation with offset and azimuth for generally anisotropic media

The Fourier series equation 14 is derived for the case of HTI media. These results can be extended to a general anisotropy by rearranging the Pšenčík and Martins (2001) linearized P-wave AVAz reflectivity (equation 1) in terms of sine and cosine functions, or

$$R(\phi,\theta) = u_0(\theta) + v_2(\theta)\sin(2\phi) + u_2(\theta)\cos(2\phi) + v_4(\theta)\sin(4\phi) + u_4(\theta)\cos(4\phi), \tag{26}$$

where

$$u_0(\theta) = w_{00} + w_{10}\sin^2\theta + w_{20}\sin^2\theta\tan^2\theta, \tag{27}$$

$$v_2(\theta) = w_{11}\sin^2\theta + w_{21}\sin^2\theta\tan^2\theta, \tag{28}$$

$$u_2(\theta) = w_{12}\sin^2\theta + w_{22}\sin^2\theta\tan^2\theta, \tag{29}$$

$$v_4(\theta) = w_{23}\sin^2\theta\tan^2\theta, \tag{30}$$

and

$$u_4(\theta) = w_{24}\sin^2\theta\tan^2\theta. \tag{31}$$

The w_{ij} coefficients are linear combinations of the weak anisotropy parameters defined by Pšenčík and Gajewski (1998) and given in Appendix A. By using transforms 24 and 25, equation 26 can be rewritten in terms of magnitude and phase so it has the same form as equation 14. To a linear approximation, the P-wave AVAz for all forms of anisotropy can be written either as equation 14 or 26. Due to reciprocity, the general P-wave AVAz expression is an even function with respect to azimuth. The fact that there are just three nonzero magnitude terms arises from the linearization used in the derivation. In an orthorhombic modeling study, Sayers and Dean (2001) report some energy on the sixth FC, but this energy was much smaller than the $n = 0$, 2, and 4 FCs, suggesting this approximation is adequate in practice.

Without going into the exact details of the expressions for the coefficients, there are several observations that can be made. For all types of anisotropy, the $n = 0$ FC (equation 27) has the same form as the three-term AVO expression (equation 1). The presence of anisotropy changes the definitions of the A, B, and C parameters from their isotropic forms. The phase of the fourth FC is independent of the angle of incidence. This is due to the fact that the $n = 4$ FCs (equations 30 and 31) are functions of a single variable, w_{23} and w_{24}, respectively, and when substituted into equation 25, results in a phase expression that is independent of the incidence angle. In contrast, the $n = 2$ FCs (equations 28 and 29) have a more complex form that results in a phase expression for the second FC, which is dependent on the angle of incidence.

The type of anisotropy governs the form and values of the individual FCs. For example, in layered HTI media that share the same symmetry azimuth, the phase of the second and fourth FC is ϕ_{sym}. In layered HTI media

in which the symmetry planes change across the interface, the phase of the second FC is dependent on the angle of incidence and is different from the phase of the fourth FC. Thus, it should be possible by observing the phase of the second and fourth FCs as function of incidence angle to determine if the layered HTI media has a consistent symmetry axis, and thus the applicability of the HTI Rüger equation.

The sine and cosine weights (equations 27–31) parameterizing the Fourier series (equation 26) are a function of nine parameters, including the density. In the case of general anisotropy, there are a total of 22 parameters (21 stiffness coefficients and density), and thus, the general inverse problem is underdetermined. This is true for orthorhombic and simpler symmetries. For this reason, it is advantageous to introduce rock physics models to reduce the number of unknown parameters.

Linear slip theory

LS theory (Schoenberg, 1980) provides a framework to model the effective medium of a fractured rock. The total compliance of the rock $\mathbf{S}$ is the sum of the background compliance $\mathbf{S}_b$ plus the compliance due to the fractures $\mathbf{S}_f$. The fractures are modeled as an imperfectly bonded interface in which the traction is continuous but the displacement might be discontinuous. The displacement discontinuity is linearly related to the traction. For example, the displacement discontinuity normal to the fracture is proportional to the normal stress. This proportionality constant is the normal fracture compliance B_N. The vertical and horizontal fracture compliances B_V and B_H are defined in a similar fashion. If the fractures are rotationally invariant, such as penny-shaped fractures, then the vertical and horizontal fracture compliances are the same. In an isotropic background, a vertical penny-shaped fracture gives rise to HTI anisotropy (Schoenberg and Sayers, 1995). When B_V and B_H are different, the fracture is asymmetric. This is probably the more realistic case (Far, 2011), but it requires an additional parameter adding complexity. Asymmetric fractures give rise to orthorhombic anisotropy.

The actual fracture compliance values depend on the size and the spatial distribution of the fractures (Worthington, 2007). Measurements of these values have been performed at different scales including laboratory measurements (Pyrak-Nolte et al., 1990), borehole sonic (Lubbe and Worthington, 2006), vertical seismic profiles (Worthington and Hudson, 2000), and microseismic (Baird et al., 2013). Verdon and Wüstefeld (2013) summarize the published values of the normal to tangential fracture compliance values.

Rather than working with fracture compliances, it is more intuitive to work with the dimensionless fracture weakness parameters. The normal, vertical, and horizontal fracture weakness parameters are, respectively,

$$\delta_N = (c_{11_b} B_N)/(1 + c_{11_b} B_N), \tag{32}$$

$$\delta_V = (c_{44_b} B_V)/(1 + c_{44_b} B_V), \tag{33}$$

and

$$\delta_H = (c_{66_b} B_H)/(1 + c_{66_b} B_H), \tag{34}$$

where c_{ij_b} are the background stiffness coefficients. In the case of an isotropic background medium, with background P- and S-wave velocities α and β, then $c_{11_b} = \rho\alpha^2$ and $c_{44_b} = \rho\beta^2$. The fractional weakness parameters range from 0 to 1. In the case in which fracture weaknesses are zero, the fracture has no influence on the total compliance. The notation is potentially confusing because the fracture weakness parameters and Thomsen parameters use δ. However, the weaknesses always have a subscript.

Single set of vertical fractures in isotropic background media

Following Appendix B, the linearized AVAz reflectivity for the case of a single set of vertical fractures with normal ϕ_{sym} in an isotropic background media may be written as the Fourier series equation 14 with magnitudes

$$r_0(\theta) = A_0 + B_0 \sin^2\theta + C_0 \sin^2\theta \tan^2\theta, \tag{35}$$

$$r_2(\theta) = \frac{1}{2}\bar{g}(\Delta\delta_V - \bar{\chi}\Delta\delta_N)\sin^2\theta + \frac{1}{2}\bar{g}(\bar{g} - 1)\Delta\delta_N \sin^2\theta \tan^2\theta, \tag{36}$$

$$r_4(\theta) = \frac{\bar{g}}{8}(\Delta\delta_H - \bar{g}\Delta\delta_N)\sin^2\theta \tan^2\theta, \tag{37}$$

and phase $\phi_n(\theta) = \phi_{\text{sym}}$. The parameter $g = \beta^2/\alpha^2 = c_{44_b}/c_{33_b}$, while $\chi = 1 - 2g$. These results are consistent with Shaw and Sen (2006). In general, VFI media are orthorhombic, but in the special case of rotationally invariant fractures, the media are HTI. The parameters describing the average AVO (equation 35) have the same form as the isotropic definitions (equations 2–4) but are perturbed by the fracture weakness parameters and are listed in Appendix B.

The azimuthal response is controlled by the $n = 2$ and $n = 4$ FCs (equations 36 and 37). Under the VFI assumption, the presence of sinusoids with periodicity of $n = 2$ and $n = 4$ implies that the media is fractured. The $n = 2$ and $n = 4$ FCs controlling the azimuthal response have the same form as the HTI case (equations 16 and 17). Based on the similarity of forms, the anisotropic gradient in VFI media, given by

$$B_{\text{ani}}^{\text{VFI}} = \bar{g}(\Delta\delta_V - \bar{\chi}\Delta\delta_N), \tag{38}$$

is a weighted difference of the vertical and normal fracture weakness parameters. As such, the possibility

exists that the anisotropic gradient $B_{\text{ani}}^{\text{VFI}}$ is zero even in the case of a fractured medium. The scaled magnitude of the fourth FC,

$$\kappa = \bar{g}(\Delta\delta_H - \bar{g}\Delta\delta_N), \tag{39}$$

is a weighted difference of the horizontal and normal fracture weakness parameters and may be used in combination with the anisotropic gradient $B_{\text{ani}}^{\text{VFI}}$ to detect the presence of fractures. Because $B_{\text{ani}}^{\text{VFI}}$ and κ are weighted differences, their interpretation is more complicated than if they were a function of a single fracture parameter. An incompressible fluid filling the fracture lowers the normal fracture weakness but does not influence the tangential fracture weakness (Bakulin et al., 2000). In the extreme case, when δ_N goes to zero, $B_{\text{ani}}^{\text{VFI}}$ is proportional to the vertical fracture weakness. The weight χ is always smaller than one, so δ_V is weighted more than δ_N.

Bakulin et al. (2000) show that to a linear approximation $\eta^{(v)} = 2\ g(\delta_V - g\delta_N)$ so that, in the case of rotationally invariant fractures, κ is a measure of anellipticity. In the case of asymmetric fractures, the ratio of the horizontal to vertical compliances B_H/B_V controls the relative magnitudes of the second and fourth FCs. The HTI parameters in Tables 1 and 2 are generated from the VFI models detailed in Tables 3 and 4 assuming rotationally invariant fractures. Note that the only difference between the two models is the value of the normal fracture weakness. This one difference gives rise to different AVO classes and AVAz responses. Figure 5

Table 3. Fracture weakness parameters used to generate the anelliptic model (Table 1).

Layer	V_{P0} (m/s)	V_{S0} (m/s)	ρ (kg/m^3)	δ_N	δ_T
1	3800	1900	2450	0	0
2	4200	2100	2550	0.09091	0.2

Table 4. Fracture weakness parameters used to generate the elliptical model (Table 2).

Layer	V_{P0} (m/s)	V_{S0} (m/s)	ρ (kg/m^3)	δ_N	δ_T
1	3800	1900	2450	0	0
2	4200	2100	2550	0.5	0.2

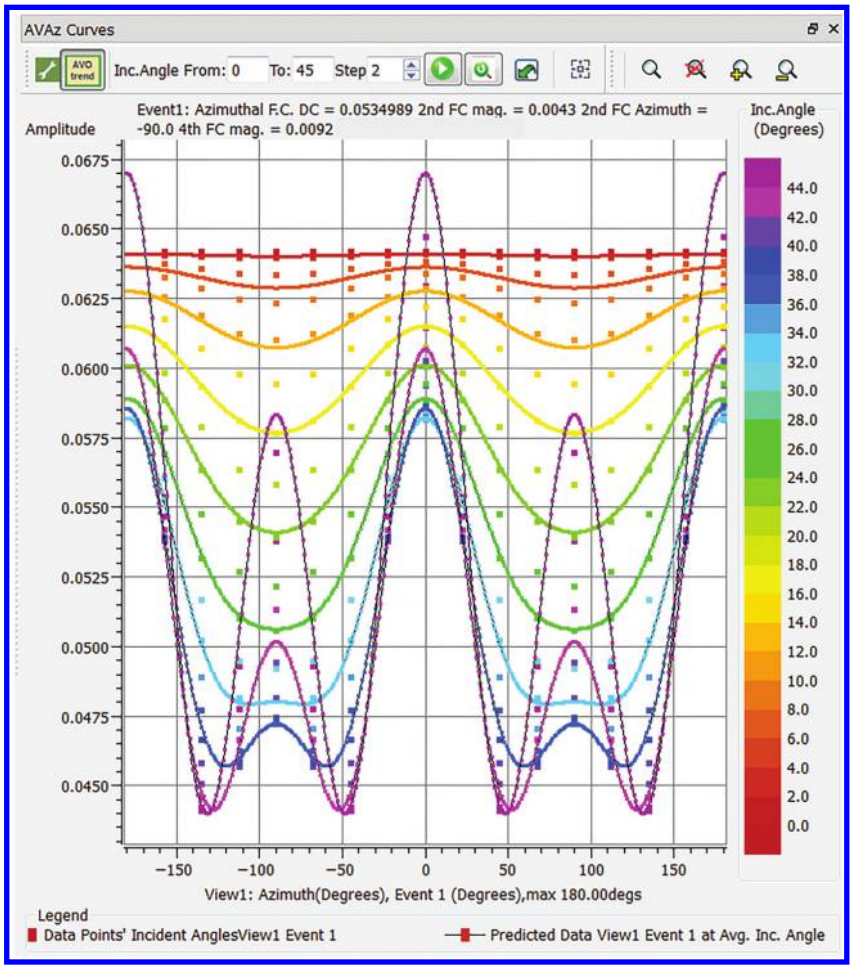

Figure 5. The AVAz response generated by the anisotropic Zoeppritz equation (Schoenberg and Protázio, 1992) from the parameters in Table 3 and a B_H/B_V ratio of 2. Note the increase in the magnitude of the fourth FC compared to Figure 2c.

shows the AVAz response generated by the anisotropic Zoeppritz equation (Schoenberg and Protázio, 1992) from the orthorhombic model specified by the parameters in Table 3, using a B_H/B_V ratio of 2. Note the increase in the magnitude of the fourth FC compared to Figure 2c.

The anisotropic gradient may be estimated from the magnitude of the second FC by rearranging equation 20 to solve explicitly for the anisotropic gradient:

$$B_{\text{ani}} \approx \frac{2}{\sin^2\theta} r_2(\theta). \tag{40}$$

The B_{ani} estimate is simply a scaled version of the magnitude of the second FC calculated at some incidence angle. Ideally, only azimuthal data from one incident angle are used to calculate the magnitude using equations 24, 28, and 29, but in practice, a range of angles must be chosen to obtain sufficient sampling and fold. Estimating B_{ani} using equation 40 becomes unstable at small angles. At larger angles, the full-offset equation 16 or 36 should be used. Estimating the magnitude using equation 24 involves taking a square root, introducing the same sign and azimuth ambiguity as the near-offset Rüger equation.

The estimation of the anisotropic gradient using equation 40 is illustrated with a northwest Louisiana 3D data set for which the main target is the Haynesville. The Haynesville Formation is a black organic-rich shale of Upper Jurassic age, which overlies the Smackover Formation. Sena et al. (2011) and Castillo et al. (2014) describe this data set in greater detail.

Figure 6 shows a comparison of the anisotropic gradient estimated using equation 40 versus equation 10 on an inline through one of the wells in this data set. The azimuthal FC estimate (equation 40) is only analyzing how the data from a 20° to a 30° incidence angle varies as a function of azimuth. The near-offset Rüger estimate (equation 10) analyzes how the data vary as function of offset and azimuth using incidence angles from 0° to 30°. The two anisotropic gradient estimates show anomalies at the top and base of the Haynesville at the well location. The base of the Haynesville is easier to pick because of the large contrast in impedance going from the Haynesville shale into the Smackover. The Haynesville top is approximately 20 ms above the base.

The estimate from the second FC (equation 40) is relatively simple to quality control. Figure 7 shows the azimuthal data displayed at the well location for incidence

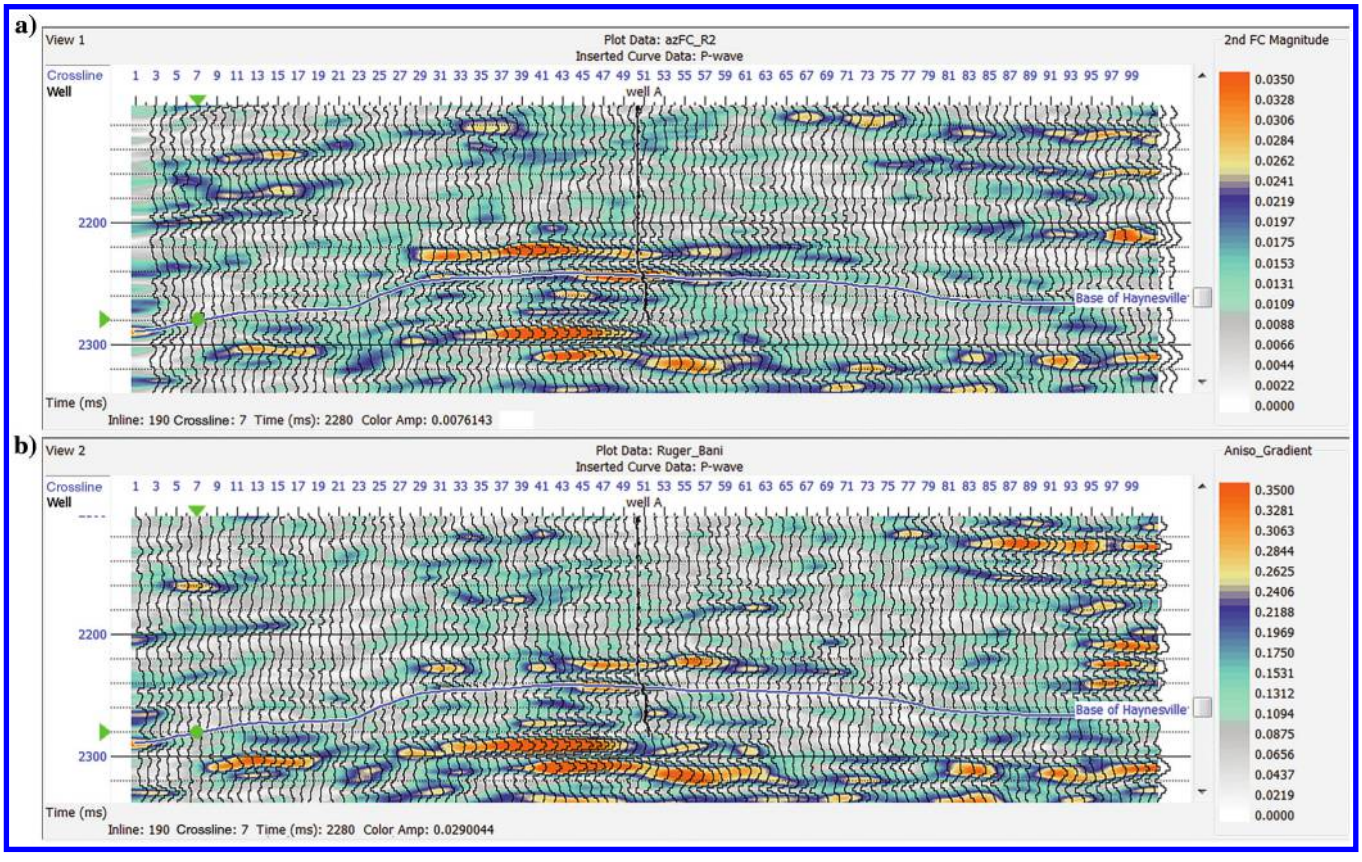

Figure 6. Panel (a) shows the anisotropic gradient estimated from the magnitude of the second FC, whereas panel (b) shows the anisotropic gradient estimated by inverting equation 10. The estimate based on the second FC uses incidence angles from 20° to 30°, whereas the estimate based on equation 10 uses angles from 0° to 30°. The two figures share many similarities and some differences. Both show anomalies at the top and base of the Haynesville. The top is approximately 20 ms above the base of the Haynesville horizon.

angles from 20° to 25° at the zone of interest. Figure 7a shows the AVAz decomposed into its constituent sinusoids. The magnitude of the second FC can be roughly estimated by just measuring the distance between the peak and the trough and dividing by two (Figure 7b). Similarly, the azimuth is estimated by just observing the phase of the trough of the sinusoid. If the anisotropic gradient is positive, then this phase corresponds to the isotropy plane azimuth. If B_{ani} is negative, this corresponds to the symmetry axis azimuth. In this case, having assumed that the anisotropic gradient is positive, the magnitude is 0.051 and the isotropy plane azimuth is −80° from north. Determining these parameters for the near-offset Rüger equation (equation 10) is more difficult because this involves solving a four-parameter nonlinear inversion problem.

To reduce the impact of the azimuth ambiguity, the isotropy plane azimuth is typically displayed on a seismic horizon in which the sign of B_{ani} is assumed to be invariant. Further, the azimuth is only shown when the size of the anisotropic gradient exceeds some threshold. This reduces the chance of the azimuth switching its orientation 90° as B_{ani} goes to zero and the chance of a polarity reversal increases. The magnitude and azimuthal information is used to construct the glyph display shown in Figure 8. The size of the glyphs is proportional to the anisotropic gradient (magnitude), whereas the orientation is controlled by the isotropy plane azimuth. The long axis of the glyphs shows the fracture strike and is consistent with the east–west principal stress in the area (Sena et al., 2011).

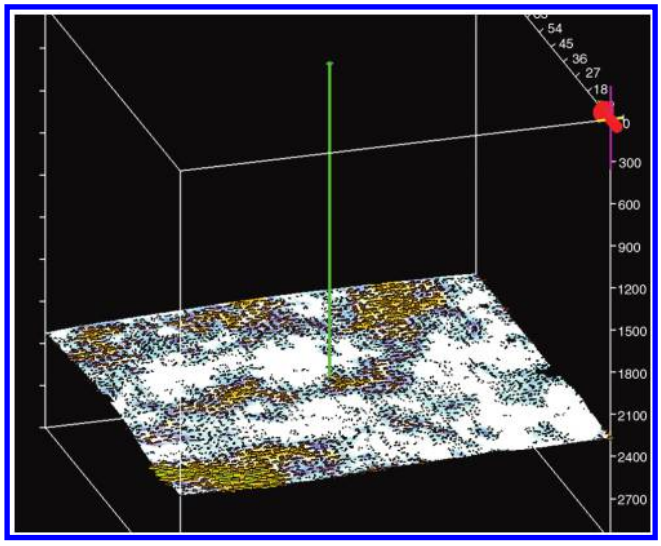

Figure 8. The size of each glyph is proportional to the anisotropic gradient, and its orientation is determined by the isotropy plane azimuth. Their directions are roughly parallel to the dominant east–west stress orientation. The anisotropic gradient is displayed in color using a similar scale as in Figure 6. The red arrow points to the north.

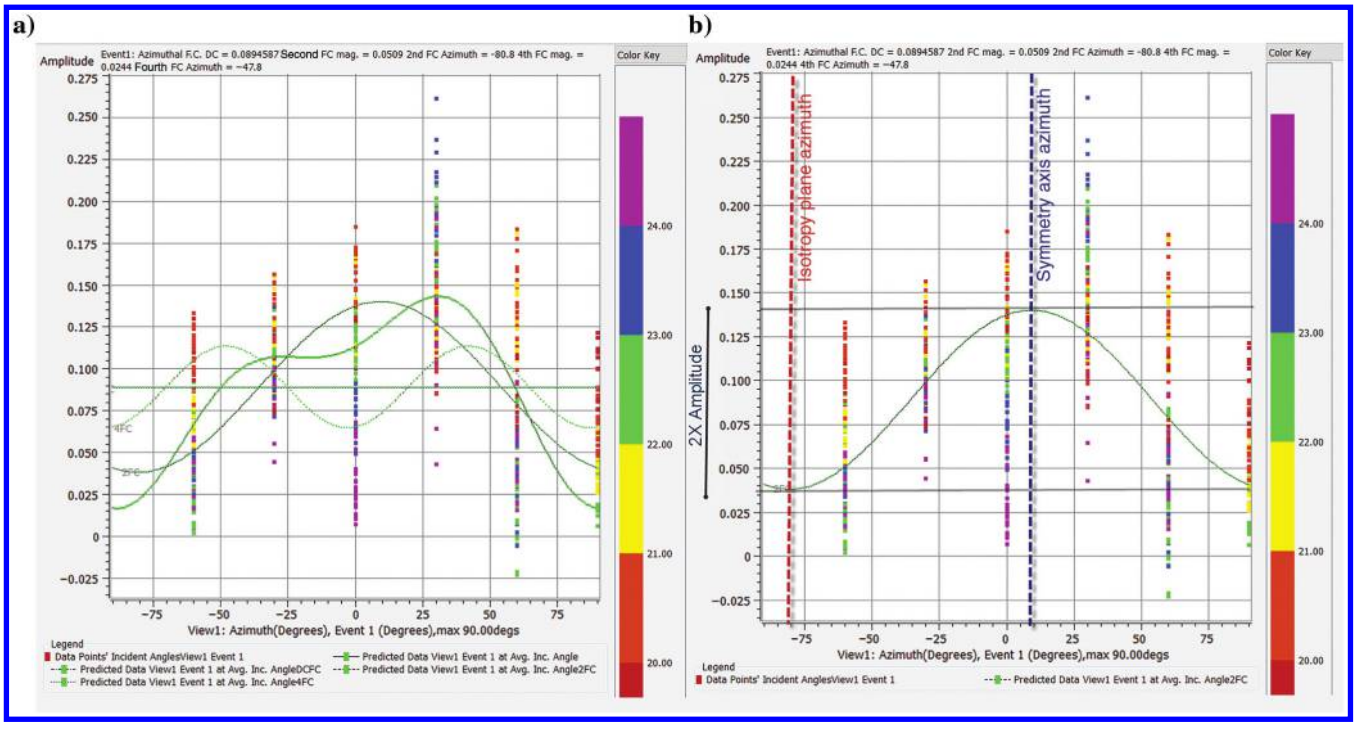

Figure 7. The AVAz data plotted for incidence angles from 20° to 25° at the well location and the base of Haynesville. Note that even for this limited angle range, there is dispersion introduced due to the AVA. The data are displayed as colored squares, with the color representing the incidence angle. The AVA dispersion is evident as vertical bars for the analyzed sectors at −60, −30, 0°, 30°, 60°, and 90°. Panel (a) shows the best fit $n = 0$, 2, and 4 sinusoids along with their sum for the average incidence angle of 22.5°. Panel (b) shows only the $n = 2$ sinusoid. The isotropy plane azimuth at −80° north corresponds to the azimuth of the trough of the sinusoid. The half-distance between the peak and trough corresponds to the magnitude of 0.051.

Single set of vertical fractures in transverse anisotropic media

In the preceding section, the background media is assumed to be isotropic; yet, the Haynesville shale is known to be VTI (Sondergeld and Rai, 2011). This last section explores the influence of a TI background on the AVAz response due to fractures. Appendix C derives the P-wave AVAz reflectivity for VFTI media, under the assumption that each fracture has the same normal ϕ_{sym}. The result of this derivation is again the Fourier series described by equation 14. Due to the assumption of the aligned fractures, the phase $\phi_2 = \phi_4 = \phi_{\text{sym}}$. The $n = 0$ magnitude in VFTI media is once again described by the AVO equation

$$r_0(\theta) = A_0 + B_0 \sin^2\theta + C_0 \sin^2\theta \tan^2\theta, \tag{41}$$

where the parameters A_0, B_0, and C_0 (equations C-7–C-9) are similar to VTI media but with an additional perturbation due to the fracture weakness parameters.

The azimuthal response is controlled by the second and fourth FCs in which the magnitude of the second FC is expressed as

$$r_2(\theta) = \frac{1}{2} B_{\text{ani}}^{\text{VFTI}} \sin^2\theta + \frac{1}{2}(1+2\bar{\varepsilon})\bar{g}(\bar{g}-1)\Delta\delta_N \sin^2\theta \tan^2\theta. \tag{42}$$

Similar to the VFI case, the VFTI anisotropic gradient

$$B_{\text{ani}}^{\text{VFTI}} = \bar{g}\left(\Delta\delta_V - \frac{(1+2\bar{\gamma})}{(1+2\bar{\varepsilon})}(\bar{\chi}+\bar{\delta})\Delta\delta_N\right). \tag{43}$$

is a weighted difference of the vertical and normal fracture weaknesses. In the VFTI case, the weights are modified by the background TI anisotropy with $g = \beta^2/\alpha^2 = c_{44_b}/c_{33_b}$ and $\chi = 1 - 2g$. The weights are functions of the average parameters across the interface. This complicates the interpretation of the anisotropic gradient because the weights depend on the background media.

The fourth FC magnitude

$$r_4(\theta) = \frac{1}{8}(1+2\bar{\varepsilon})\bar{g}(\Delta\delta_H - \bar{g}\Delta\delta_N)\sin^2\theta\tan^2\theta \tag{44}$$

has the same basic form as in VFI media (equation 37), but it is scaled by an additional factor dependent on the P-wave anisotropy of the background media. Large positive values of $\bar{\varepsilon}$, such as found in shales, amplify the fourth FC. Note that each of the VFTI FCs reduces to their VFI equivalents in the case that $\bar{\varepsilon} = \bar{\delta} = \bar{\gamma} = 0$.

The linearized VFTI AVOAz reflectivity inversion problem for fractional interface properties is underdetermined for the same reason that the VTI AVO inversion problem is underdetermined. Excluding the fracture weakness parameters, there are five parameters controlling the average AVO (equation 41), but there are only three parameters that can be determined.

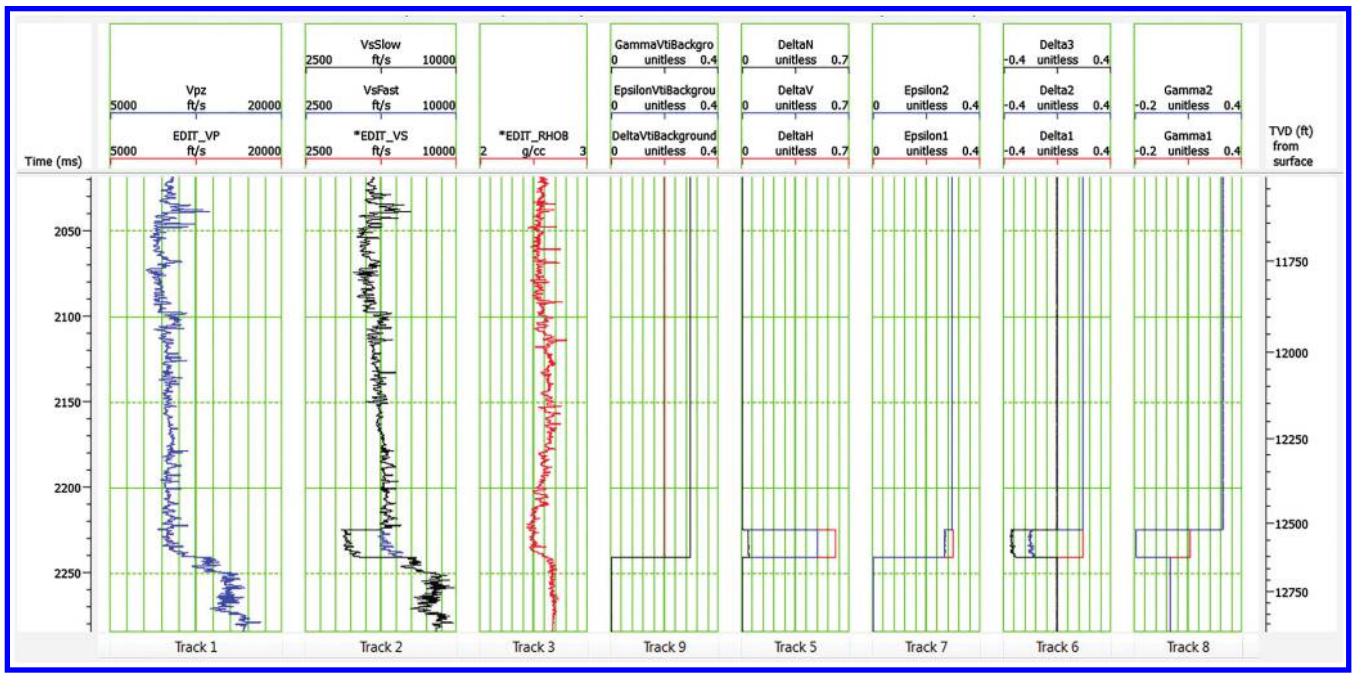

Figure 9. The anisotropic model used to generate the VFTI synthetic (Figure 13). The P-wave, S-wave, and density logs are what would be typically used to perform AVO modeling. The normal, vertical, and horizontal fracture weaknesses describe the fracture.

Modeling vertical fractures in transverse anisotropic media

The impact of a TI background media on the AVAz response is studied by performing forward modeling following Downton (2014). A 1D isotropic layered earth model is constructed in a similar fashion as in an AVO modeling study, and then, TI anisotropy is determined and incorporated in a manner analogous to Lin and Thomsen (2013). For each layer, LS theory is used to construct the anisotropic stiffness matrix due to fractures. The synthetic is generated using a convolutional modeling scheme in which the P-wave reflectivity is calculated using the Zoeppritz equation or some linearized approximation of it. The synthetic is compared to the seismic. Differences in the AVO response are used to update the background TI anisotropy whereas differences in the AVAz response are used to update the fracture model.

For the well log shown in Figure 6, only the P-wave, S-wave, and density logs are available. These logs are used to construct the background model shown in

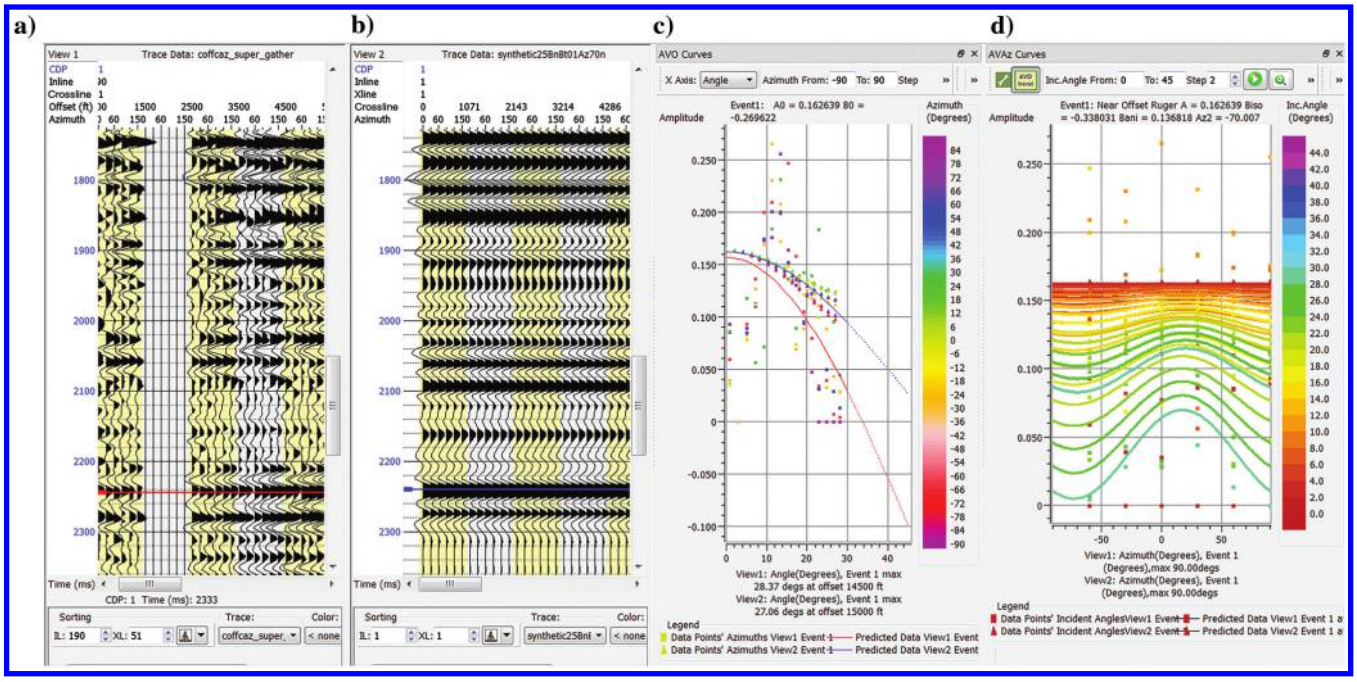

Figure 10. The (c) AVA and (d) AVAz of the (a) real and (b) VFI synthetic data plotted for the base of the Haynesville event. Note the real data have a different AVA trend than do the synthetic data. The blue AVA trend corresponds to the blue event on the synthetic data (a), whereas the red corresponds to the real data. In panels (c and d), the data plotted as squares correspond to the real data, whereas the triangles correspond to the synthetic data.

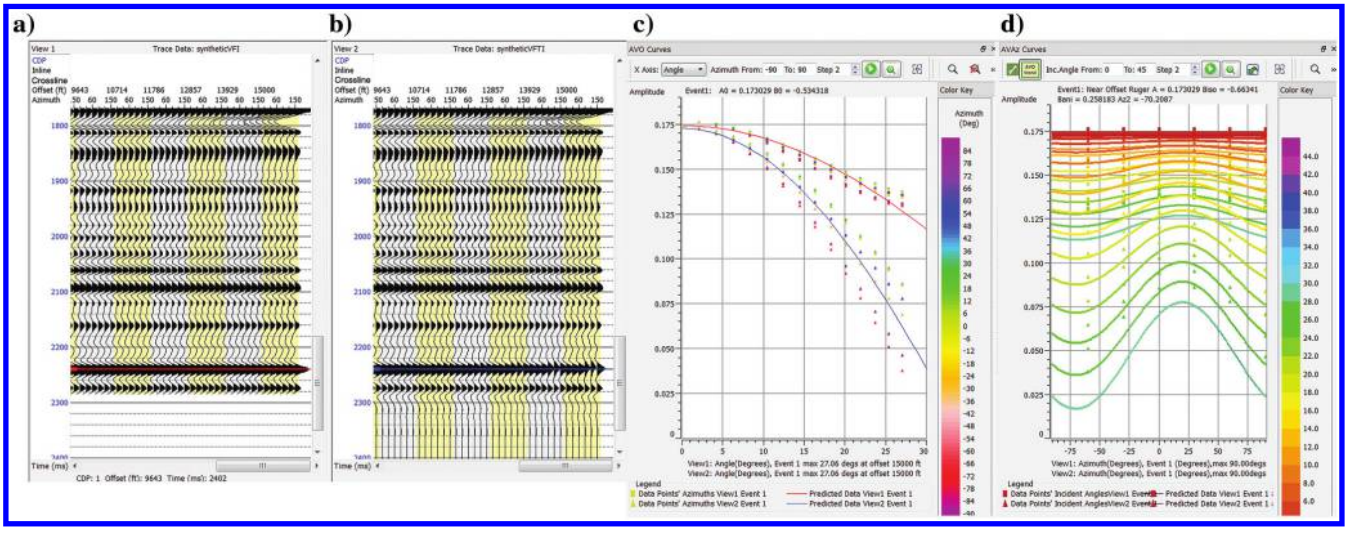

Figure 11. The (c) AVA and (d) AVAz of the (a) VFI and (b) VFTI synthetic data plotted for the base of the Haynesville event. Note how the introduction of the TI background media changes the AVA trend. The red AVA trend corresponds to the red event in panel (a), whereas the blue AVA trend corresponds to the blue event in panel (b). In panels (c and d), the VFI synthetic data are plotted as squares whereas the VFTI synthetic data are plotted as triangles.

Figure 9. To match the AVAz response shown in Figures 6 and 7, it is assumed that the Haynesville is fractured. For simplicity, a single set of rotationally invariant vertical fractures is assumed. Initially, specifying fractures with a tangential fracture weakness of $\delta_T = 0.2$ and ratio $B_N/B_T = 0.1$ results in the synthetic shown in Figure 10. This figure compares the synthetic to the real data AVO and AVAz at the base of Haynesville.

The fact that the synthetic data exhibit a slightly different AVO trend to the real data is used to determine the VTI parameters following the work of Lin and Thomsen (2013). The Smackover Formation is assumed to be isotropic, whereas the Haynesville shale above is assumed to be VTI. Different combinations of δ and ε were tested to find the best match to the real data. Due to the near-offset nature of this data set (30° maximum angle), the AVO testing was most sensitive to δ with the best match being $\delta = 0.2$. The data exhibited little sensitivity to ε, so the observation of Vernik and Liu (1997) that $\varepsilon > \delta$ was used to specify $\varepsilon = 0.3$. Last, the empirical relationship $\gamma \approx -0.01 + 0.96\varepsilon$, by Wang (2002), is used to specify the value of γ. Although γ does not influence the AVO trend, it is ultimately required in the calculation of $B_{\text{ani}}^{\text{VFTI}}$. Figure 11 shows how the introduction of the TI anisotropy alters the AVO and AVAz synthetic response. The biggest impact is on the AVO. The peak-to-trough AVAz is changed lit-

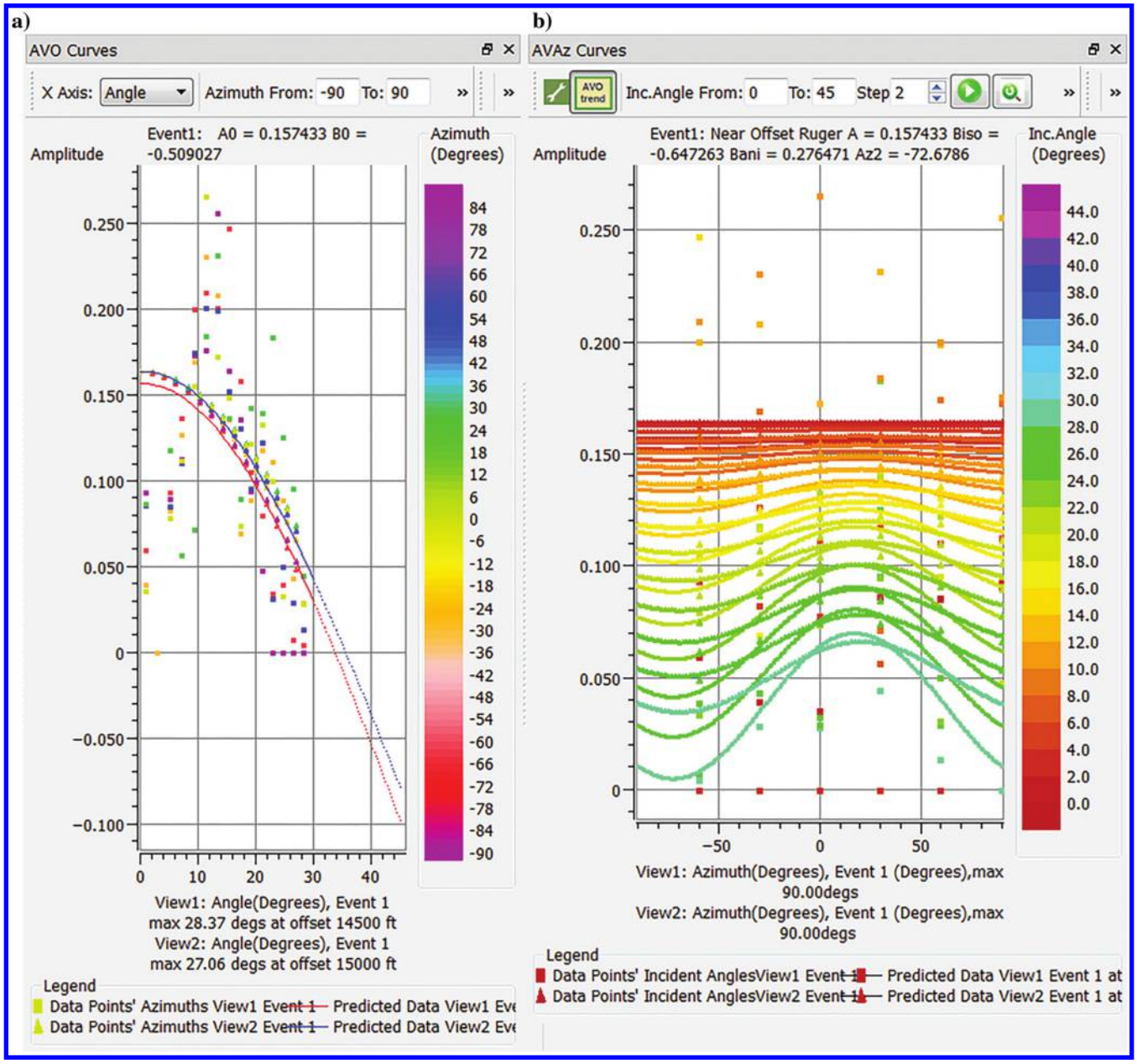

Figure 12. The (a) AVA and (b) AVAz of the real and VFTI synthetic data are plotted for the base of the Haynesville event as squares and triangles, respectively. Note that after the introduction of the TI background media, the VFTI synthetic (the blue AVA curve) shares the same AVA trend as the real data (the red AVA curve).

tle between the two models. Figure 12 shows that, after introducing the background TI anisotropy, the VFTI synthetic and real data share the same AVO trend.

Next, different combinations of δ_T and B_N/B_T were tested to obtain a better match to the AVAz of the real seismic. Initially, the value of δ_T was held constant and the B_N/B_T ratio was varied. It was possible to match the AVAz of the real data, but this required unreasonably large values of δ_N. Better results were obtained by varying δ_T and holding B_N/B_T to its initial value. Figure 13 shows a good match for the AVO and AVAz using $\delta_T = 0.5$. Figure 9 summarizes the parameters used in the construction of this synthetic. The parameters chosen in this manner are nonunique, but they prove that it is possible to model the real seismic response using geologically plausible parameters. The determination of these parameters is essentially a bootstrapping process. The fact that the AVOAz can be separated into AVO and AVAz is used to help build the model. The fracture parameters primarily control the AVAz, whereas the TI parameters control the AVO.

Discussion

The emphasis of this paper is that the AVAz can be quantified in terms of the magnitude and phase of the different FCs. This parameterization is purely descriptive. Interpretation of these parameters depends on the anisotropic symmetry class or fracture system. It is possible to invert for fracture parameters (Downton and Roure, 2010), but this makes a strong assumption about the form of the anisotropy.

If anisotropy is assumed to be due to VFI, it is also possible to invert for an unambiguous estimate of the isotropy plane azimuth (Downton et al., 2011). However, the method requires information from the fourth FC and hence far-offset data. The Haynesville example in this paper is thought to be VFTI and only includes angles up to 30°, so it is not suitable for this analysis.

Conclusion

P-wave AVOAz analysis can be separated into two parts: AVO and AVAz analyses. It is possible to detect anisotropy and fractures by just looking at the AVAz part. The AVAz may be modeled as a Fourier series or the sum of a series of sinusoids, with each sinusoid being characterized by its magnitude and phase. The FC parameterization is parsimonious. Only sinusoids with periods $n = 0$, 2, and 4 are needed to describe the AVAz for the case of general anisotropy. The fact that only even terms are needed is because of reciprocity. The FC parameterization is descriptive. It is possible to graph these sinusoids and estimate their amplitude and phase by hand, so it is easy to get an intuitive feel as to whether the estimated parameters are reasonable.

To understand the significance of the parameters, some anisotropic or fracture system must be assumed. The cases of HTI, VFI, and VFTI media were studied. In each case, if the media has the same mirror planes, the phase of the second and fourth FCs is the same. If the phase is different, it suggests that this assumption is violated. In all the studied media, the magnitude of the second FC can be used to approximate the anisotropic gradient and give results similar to inverting the near-offset Rüger equation. Interpretation of the anisotropic gradient changes depending on the type of media. In HTI media, the anisotropic gradient is a weighted differ-

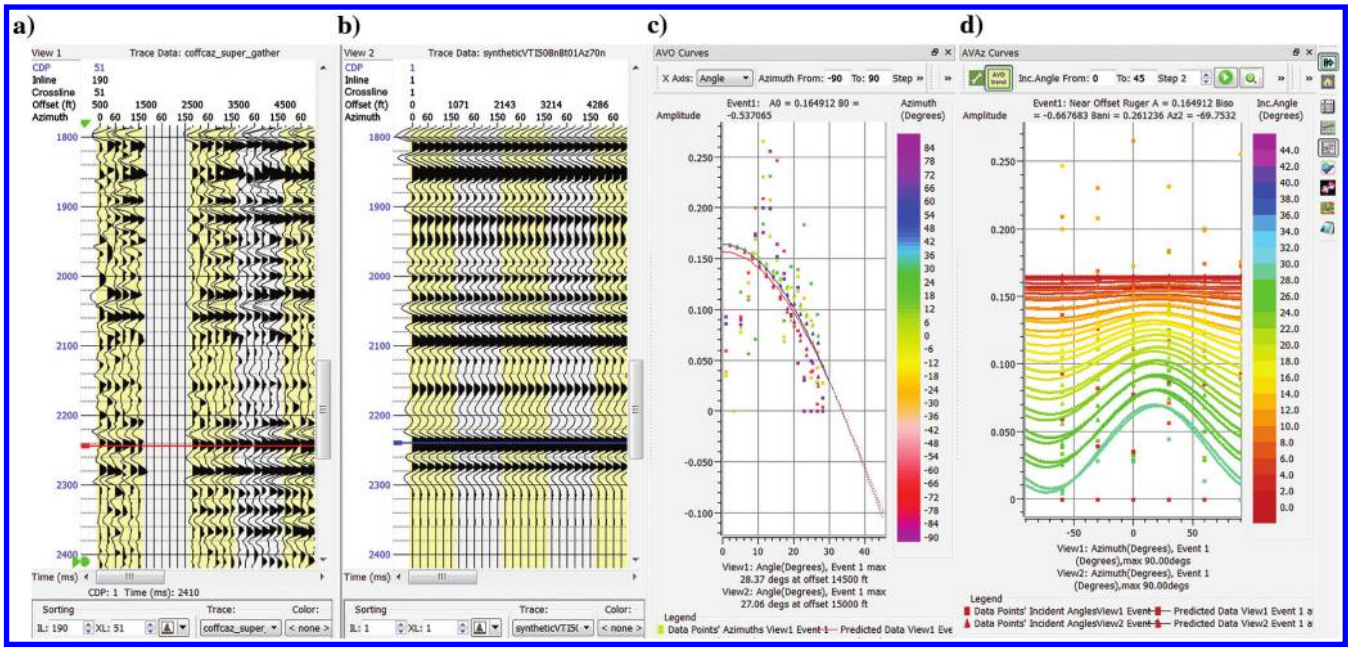

Figure 13. The (c) AVA and (d) AVAz of (a) the real and (b) the updated VFTI synthetic data are plotted for the base of the Haynesville event as squares and triangles, respectively. Note that after the fracture parameters are adjusted, the two share similar AVA and AVAz trends.

ence of Thomsen parameters and is a measure of anisotropy. In VFI and VFTI media, the anisotropic gradient is a weighted difference of fracture parameters whose weights depend on the background media. Thus, the anisotropic gradient is a measure of the fracture parameters whose interpretation changes, depending on the background media.

In HTI media, the magnitude of the fourth FC can be used to study anellipticity. In VFI and VFTI media, the magnitude of the fourth FC is also a weighted difference of the fracture parameters, and hence, it is an indicator of fractures. In orthorhombic media, due to asymmetric vertical fractures in a background isotropic media, the ratio of the horizontal to vertical compliances controls the relative size of the fourth FC, the size of which can be much larger than in an HTI medium. In VFTI media, the background P-wave anisotropy also influences the magnitude of the fourth FC.

Acknowledgments

The authors thank CGG Multi-Client and New Ventures for permission to show this data. We thank G. Castillo, S. Voisey, and K. Chesser of CGG for help with the 3D data set. In addition, we thank B. Russell, D. Hampson, A. Marcus, D. Schmidt, and A. Veronesi of CGG for support they gave in creating this work. Lastly, we thank F. Mahmoudian and two other anonymous reviewers for their constructive feedback helping to make this a better paper.

Appendix A

Amplitude-variation-offset-and-azimuth weights for general anisotropy

The weights w_{ij} parameterizing the FCs for general anisotropy (equations 27–31) are

$$w_{00} = A_{\text{iso}} + \frac{1}{2\alpha^2}\Delta(\alpha^2\varepsilon_z), \tag{A-1}$$

$$w_{10} = B_{\text{iso}} + \frac{1}{4\alpha^2}[\Delta(\alpha^2\delta_x) - 8\Delta(\beta^2\gamma_x)] + \frac{1}{4\alpha^2}[\Delta(\alpha^2\delta_y) - 8\Delta(\beta^2\gamma_y)] - \frac{1}{2\alpha^2}\Delta(\alpha^2\varepsilon_z), \tag{A-2}$$

$$w_{20} = C_{\text{iso}} + \frac{1}{16\alpha^2}[3\Delta(\alpha^2\varepsilon_x) + 3\Delta(\alpha^2\varepsilon_y) + \Delta(\alpha^2\delta_z)], \tag{A-3}$$

$$w_{11} = \frac{1}{2\alpha^2}[\Delta(\alpha^2\chi_z) - 4\Delta(\beta^2\varepsilon_{45})], \tag{A-4}$$

$$w_{12} = \frac{1}{4\alpha^2}[\Delta(\alpha^2\delta_x) - 8\Delta(\beta^2\gamma_x) - (\Delta(\alpha^2\delta_y) - 8\Delta(\beta^2\gamma_y))], \tag{A-5}$$

$$w_{21} = \frac{1}{4\alpha^2}[\Delta(\alpha^2\varepsilon_{16}) + \Delta(\alpha^2\varepsilon_{26})], \tag{A-6}$$

$$w_{22} = \frac{1}{4\alpha^2}[\Delta(\alpha^2\varepsilon_x) - (\Delta\alpha^2\varepsilon_y)], \tag{A-7}$$

$$w_{23} = \frac{1}{8\alpha^2}[\Delta(\alpha^2\varepsilon_{16}) - \Delta(\alpha^2\varepsilon_{26})], \tag{A-8}$$

$$w_{24} = \frac{1}{16\alpha^2}[\Delta(\alpha^2\varepsilon_x) + \Delta(\alpha^2\varepsilon_y) - \Delta(\alpha^2\delta_z)], \tag{A-9}$$

and they are expressed in terms of the weak anisotropy parameters defined by Pšenčik and Gajewski (1998) in equation 17b. Equation 27 is evaluated with reference to some background P-wave velocity α and S-wave velocity β. By choosing these background velocities to be the average background velocities of the two media generating the reflectivity, the definitions of A, B_{iso}, and C_{iso} are consistent with equations 2–4 calculated using the isotropic velocities.

Appendix B

Amplitude-variation-offset-and-azimuth in vertical fractures in an isotropic media

Appendix B outlines the derivation of AVAz reflectivity expression for a single set of VFI background medium. The stiffness matrix for a single vertical fracture perpendicular to the x-axis in a background isotropic medium is (Schoenberg and Douma, 1988) given as

$$\mathbf{C} = \begin{bmatrix} M(1-\delta_N) & \lambda(1-\delta_N) & \lambda(1-\delta_N) & 0 & 0 & 0 \\ \lambda(1-\delta_N) & M(1-\chi^2\delta_N) & \lambda(1-\chi\delta_N) & 0 & 0 & 0 \\ \lambda(1-\delta_N) & \lambda(1-\chi\delta_N) & M(1-\chi^2\delta_N) & 0 & 0 & 0 \\ 0 & 0 & 0 & \mu & 0 & 0 \\ 0 & 0 & 0 & 0 & \mu(1-\delta_V) & 0 \\ 0 & 0 & 0 & 0 & 0 & \mu(1-\delta_H) \end{bmatrix}, \tag{B-1}$$

where $\chi = 1 - 2g$ and $g = \mu/M = c_{44_b}/c_{33_b}$. The parameter g can also be expressed in terms of the background P-wave velocity α and the S-wave velocity β as $g = \beta^2/\alpha^2$, which for the isotropic background medium is directionally invariant. The azimuthal Fourier series described by equations 27–31 is calculated by substituting the density normalized stiffness values obtained from matrix B-1 into the w_{ij} coefficients (equations A-1–A-9) using the background isotropic P- and S-wave velocities as the reference velocities. The resulting expressions are then rearranged as the truncated Fourier series:

$$R(\phi,\theta) = r_0(\theta) + r_2(\theta)\cos(2\phi) + r_4(\theta)\cos(4\phi). \tag{B-2}$$

Matrix B-1 is written so that the normal of the fracture is the x-axis. To generalize this to any orientation, the fracture may be rotated anticlockwise ϕ_{sym} about the z-axis by performing a change of variables $\phi \rightarrow (\phi - \phi_{\text{sym}})$ so that equation B-2 becomes

$$R(\phi,\theta) = r_0(\theta) + r_2(\theta)\cos(2(\phi-\phi_{\text{sym}})) + r_4(\theta)\cos(4(\phi-\phi_{\text{sym}})), \tag{B-3}$$

which has the same form as equation 14. In this case, the magnitudes are

$$r_0(\theta) = A_0 + B_0\sin^2\theta + C_0\sin^2\theta\tan^2\theta, \tag{B-4}$$

$$r_2(\theta) = \frac{1}{2}\bar{g}(\Delta\delta_V - \bar{\chi}\Delta\delta_N)\sin^2\theta + \frac{1}{2}\bar{g}(\bar{g}-1)\Delta\delta_N\sin^2\theta\tan^2\theta, \tag{B-5}$$

$$r_4(\theta) = \frac{\bar{g}}{8}(\Delta\delta_H - \bar{g}\Delta\delta_N)\sin^2\theta\tan^2\theta, \tag{B-6}$$

and phase $\phi_n(\theta) = \phi_{\text{sym}}$. The terms describing the AVA equation B-4

$$A_0 = A_{\text{iso}} - \frac{1}{4}\bar{\chi}^2\Delta\delta_{\text{N}}, \tag{B-7}$$

$$B_0 = B_{\text{iso}} + \frac{\bar{g}}{2}\Delta\delta_{\text{V}} - \frac{\bar{\chi}}{4}\Delta\delta_{\text{N}}, \tag{B-8}$$

and

$$C_0 = C_{\text{iso}} - \frac{\bar{g}}{8}\Delta\delta_{\text{H}} - \frac{1}{8}(3\bar{g}^2 - 4\bar{g} + 2)\Delta\delta_{\text{N}} \tag{B-9}$$

are perturbed from the isotropic equations 2–4 by the fracture weakness parameters. The velocities used in calculating the isotropic reflectivity are the isotropic background velocities.

Appendix C

Amplitude-variation-offset-and-azimuth in vertical fractures in a transverse isotropic media

Appendix C outlines the derivation of AVAz reflectivity expression for a single set of VFTI background medium. The density-normalized stiffness matrix for a single set of parallel vertical fractures perpendicular to the x-axis in a background TI media is (Schoenberg and Helbig, 1997)

$$\mathbf{A} = \begin{bmatrix} a_{11_b}(1-\delta_N) & a_{12_b}(1-\delta_N) & a_{13_b}(1-\delta_N) & 0 & 0 & 0 \\ a_{12_b}(1-\delta_N) & a_{11_b}\left(1-\frac{a_{12_b}^2}{a_{11_b}^2}\delta_N\right) & a_{13_b}\left(1-\frac{a_{12_b}}{a_{11_b}}\delta_N\right) & 0 & 0 & 0 \\ a_{13_b}(1-\delta_N) & a_{13_b}\left(1-\frac{a_{12_b}}{a_{11_b}}\delta_N\right) & a_{33_b}\left(1-\frac{a_{13_b}^2}{a_{11_b}a_{33_b}}\delta_N\right) & 0 & 0 & 0 \\ 0 & 0 & 0 & a_{44_b} & 0 & 0 \\ 0 & 0 & 0 & 0 & a_{44_b}(1-\delta_V) & 0 \\ 0 & 0 & 0 & 0 & 0 & a_{66_b}(1-\delta_H) \end{bmatrix} \tag{C-1}$$

with the constraint $a_{12_b} = a_{11_b} - 2a_{66_b}$. The density-normalized background stiffness coefficients a_{33b} and a_{44b} are used to define the background P-wave velocity $\alpha = \sqrt{a_{33_b}}$ and S-wave velocity $\beta = \sqrt{a_{44_b}}$ used in the derivation. Similar to the VFI derivation, the variables $g = a_{44_b}/a_{33_b}$ and $\chi = 1 - 2g$ are defined. The matrix C-1 is rewritten in terms of Thomsen's parameters by substituting

$$f = a_{11_b}/a_{33_b} = (1+2\varepsilon), \tag{C-2}$$

$$\zeta = a_{12_b}/a_{33_b} = f - 2d, \tag{C-3}$$

$$\xi = a_{13_b}/a_{33_b} \approx \chi + \delta, \tag{C-4}$$

and

$$d = a_{66_b}/a_{33_b} = (1+2\gamma)g, \tag{C-5}$$

into matrix C-1 as

$$\mathbf{A} = a_{33_b}\begin{bmatrix} f(1-\delta_N) & \zeta(1-\delta_N) & \xi(1-\delta_N) & 0 & 0 & 0 \\ \zeta(1-\delta_N) & f\left(1-\frac{\zeta^2}{f^2}\delta_N\right) & \xi\left(1-\frac{\zeta}{f}\delta_N\right) & 0 & 0 & 0 \\ \xi(1-\delta_N) & \xi\left(1-\frac{\zeta}{f}\delta_N\right) & \left(1-\frac{\xi^2}{f}\delta_N\right) & 0 & 0 & 0 \\ 0 & 0 & 0 & g & 0 & 0 \\ 0 & 0 & 0 & 0 & g(1-\delta_V) & 0 \\ 0 & 0 & 0 & 0 & 0 & d(1-\delta_H) \end{bmatrix}. \tag{C-6}$$

At this point, the derivation proceeds similar to the VFI derivation (Appendix B), substituting the density-normalized stiffness matrix C-6 into the w_{ij} coefficients (equations A-1–A-9), simplifying and dropping the nonlinear terms. The result is written as a Fourier series represented by equation 14 with phase $\phi_2 = \phi_4 = \phi_{\text{sym}}$. The magnitude of the $n = 0$ FC is described by the AVO equation 15 with

$$A_0 = A_{\text{VTI}} - \frac{(\bar{\chi}+\bar{\delta})^2}{4(1+2\bar{\varepsilon})}\Delta\delta_N, \tag{C-7}$$

$$B_0 = B_{\text{VTI}} + \frac{1}{2}(\bar{g}\Delta\delta_V - \frac{1}{2}(\bar{\chi}+\bar{\delta})\Delta\delta_N), \tag{C-8}$$

and

$$C_0 = C_{\mathrm{VTI}} - \frac{1}{8}(1+2\bar{\varepsilon})(\bar{g}\Delta\delta_H + (3\bar{g}^2 - 4\bar{g} + 2)\Delta\delta_N). \tag{C-9}$$

The parameters A_0, B_0, and C_0 are perturbed from the VTI case by the fracture weakness parameters. The VTI background and the fractures modify the average AVO trend compared to the isotropic case. The fractures lower the vertical P-wave velocity and, hence, change the impedance contrast at the interface. Large positive $\bar{\delta}$ values amplify this change.

The magnitude of the second FC is

$$r_2(\theta) = \frac{1}{2}B_{\mathrm{ani}}^{\mathrm{VFTI}}\sin^2\theta + \frac{1}{2}(1+2\bar{\varepsilon})\bar{g}(\bar{g}-1)\Delta\delta_N \sin^2\theta\tan^2\theta \tag{C-10}$$

with

$$B_{\mathrm{ani}}^{\mathrm{VFTI}} = \bar{g}(\Delta\delta_V - \frac{(1+2\bar{\gamma})}{(1+2\bar{\varepsilon})}(\bar{\chi}+\bar{\delta})\Delta\delta_N). \tag{C-11}$$

Lastly, the magnitude of the fourth FC is

$$r_4(\theta) = \frac{1}{8}(1+2\bar{\varepsilon})\bar{g}(\Delta\delta_H - \bar{g}\Delta\delta_N)\sin^2\theta\tan^2\theta. \tag{C-12}$$

Each of the magnitude expressions for the $n = 0$, 2, and 4 sinusoids reduce to the VFI form in the case that $\bar{\varepsilon} = \bar{\delta} = \bar{\gamma} = 0$.

References

Aki, K., and P. G. Richards, 1980, Quantitative seismology: Theory and methods: W. H. Freeman and Co.

Baird, A. F., J.-M. Kendall, J. P. Verdon, A. Wüstefeld, T. E. Noble, Y. Li, M. Dutko, and Q. J. Fisher, 2013, Monitoring increases in fracture connectivity during hydraulic stimulations from temporal variations in shear-wave splitting polarization: Geophysical Journal International, **195**, 1120–1131, doi: 10.1093/gji/ggt274.

Bakulin, A., V. Grechka, and I. Tsvankin, 2000, Estimation of fracture parameters from reflection seismic data — Part I: HTI model due to a single fracture set: Geophysics, **65**, 1788–1802, doi: 10.1190/1.1444863.

Blangy, J. P., 1994, AVO in transversely isotropic media — An overview: Geophysics, **59**, 775–781, doi: 10.1190/1.1443635.

Buland, A., and H. Omre, 2003, Bayesian linearized AVO inversion: Geophysics, **68**, 185–198, doi: 10.1190/1.1543206.

Cary, P. W., 1999, Common-offset-vector gathers: An alternative to cross-spreads for wide-azimuth 3-D surveys: 69th Annual International Meeting, SEG, Expanded Abstracts, 1496–1499.

Castillo, G., S. Voisey, K. Chesser, N. van de Coevering, A. Bouziat, G. Oliver, C. Vinh Ly, and L. Kuo, 2014, Integrating surface seismic, microseismic, rock properties and mineralogy in the Haynesville shale play: First Break, **32**, 71–81.

Downton, J., 2014, P-wave AVAz modeling: A Haynesville case study: Presented at GeoConvention.

Downton, J., and D. Gray, 2006, AVAZ parameter uncertainty estimation: 76th Annual International Meeting, SEG, Expanded Abstracts, 234–238, doi: 10.1190/1.2370006.

Downton, J., and B. Roure, 2010, Azimuthal simultaneous elastic inversion for fracture detection: 80th Annual International Meeting, SEG, Expanded Abstracts, 263–267.

Downton, J., B. Roure, and L. Hunt, 2011, Azimuthal Fourier coefficients: CSEG Recorder, **36**, 22–36.

Far, M. E., 2011, Seismic characterization of naturally fractured reservoirs: Ph.D. dissertation, University of Houston.

Gray, D., and D. Todorovic-Marinic, 2004, Fracture detection using 3D azimuthal AVO: CSEG Recorder, **29**, 5–8.

Gurevich, B., M. Pervukhina, and D. Makarynska, 2011, An analytic model for the stress-induced anisotropy of dry rocks: Geophysics, **76**, no. 3, WA125–WA133, doi: 10.1190/1.3567950.

Hudson, J. A., 1981, Wave speeds and attenuation of elastic waves in material containing cracks: Geophysical Journal of the Royal Astronomical Society, **64**, 133–150, doi: 10.1111/j.1365-246X.1981.tb02662.x.

Ikelle, L. T., 1996, Amplitude variations with azimuths (AVAZ) inversion based on linearized inversion of common azimuth sections, *in* E. Fjaer, R. Holt, and J. S. Rathore, eds., Seismic anisotropy: SEG, 601–644.

Lin, R., and L. Thomsen, 2013, Extracting polar anisotropy parameters from seismic data and well logs: 83rd Annual International Meeting, SEG, Expanded Abstracts, 310–314.

Lubbe, R., and M. H. Worthington, 2006, A field investigation of fracture compliance: Geophysical Prospecting, **54**, 319–331, doi: 10.1111/j.1365-2478.2006.00530.x.

Pšenčik, I., and D. Gajewski, 1998, Polarization, phase velocity, and NMO velocity of qP-waves in arbitrary weakly anisotropic media: Geophysics, **63**, 1754–1766, doi: 10.1190/1.1444470.

Pšenčik, I., and J. L. Martins, 2001, Properties of weak contrast PP reflection/transmission coefficients for weakly anisotropic elastic media: Studia Geophysica et Geodaetica, **45**, 176–199, doi: 10.1023/A:1021868328668.

Pyrak-Nolte, L. J., L. R. Myer, and N. G. W. Cook, 1990, Transmission of seismic waves across single natural fractures: Journal of Geophysical Research, **95**, 8617–8638, doi: 10.1029/JB095iB06p08617.

Rasolofosaon, P., 1998, Stress-induced seismic anisotropy revisited: Revue de l'Institut Francais du Petrole, **53**, 679–692, doi: 10.2516/ogst:1998061.

Rüger, A., 1998, Variation of P-wave reflectivity with offset and azimuth in anisotropic media: Geophysics, **63**, 935–947, doi: 10.1190/1.1444405.

Rüger, A., 2002, Reflection coefficients and azimuthal AVO analysis in anisotropic media: SEG, Geophysical Monograph Series 10.

Sayers, C., and S. Dean, 2001, Azimuth-dependent AVO in reservoirs containing non-orthogonal fracture sets: Geophysical Prospecting, **49**, 100–106, doi: 10.1046/j.1365-2478.2001.00236.x.

Schoenberg, M., 1980, Elastic behavior across linear slip interfaces: Journal of the Acoustical Society of America, **68**, 1516–1521, doi: 10.1121/1.385077.

Schoenberg, M., and J. Douma, 1988, Elastic wave propagation in media with parallel fractures and aligned cracks: Geophysical Prospecting, **36**, 571–590, doi: 10.1111/j.1365-2478.1988.tb02181.x.

Schoenberg, M., and K. Helbig, 1997, Orthorhombic media: Modeling elastic wave behavior in a vertically fractured earth: Geophysics, **62**, 1954–1974, doi: 10.1190/1.1444297.

Schoenberg, M., and J. Protázio, 1992, "Zoeppritz" rationalized and generalized to anisotropy: Journal of Seismic Exploration, **1**, 125–144, doi: 10.1121/1.2029011.

Schoenberg, M., and C. Sayers, 1995, Seismic anisotropy of fractured rock: Geophysics, **60**, 204–211, doi: 10.1190/1.1443748.

Sena, A., G. Castillo, K. Chesser, S. Voisey, J. Estrada, J. Carcuz, E. Carmona, and P. Hodgkins, 2011, Seismic reservoir characterization in resource shale plays: Stress analysis and sweet spot discrimination: The Leading Edge, **30**, 758–764, doi: 10.1190/1.3609090.

Shaw, R. K., and M. K. Sen, 2006, Use of AVOA data to estimate fluid indicator in a vertically fractured medium: Geophysics, **71**, no. 3, C15–C24, doi: 10.1190/1.2194896.

Sondergeld, C. H., and C. S. Rai, 2011, Elastic anisotropy of shales: The Leading Edge, **30**, 324–331, doi: 10.1190/1.3567264.

Swan, H. W., 1993, Properties of direct AVO hydrocarbon indicators, *in* J. P. Castagna, and M. M. Backus, eds., Offset-dependent reflectivity — Theory and practice of AVO analysis: SEG, Investigations in Geophysics 8, 78–92.

Thomsen, L., 1986, Weak elastic anisotropy: Geophysics, **51**, 1954–1966, doi: 10.1190/1.1442051.

Thomsen, L., 1993, Weak anisotropic reflections, *in* J. P. Castagna, and M. M. Backus, eds., Offset-dependent reflectivity — Theory and practice of AVO analysis: SEG, Investigations in Geophysics 8, 103–111.

Tsvankin, I., 2001, Seismic signatures and analysis of reflection data in anisotropic media: Elsevier Science.

Verdon, J. P., and A. Wüstefeld, 2013, Measurement of the normal/tangential fracture compliance ratio (ZN/ZT) during hydraulic fracture stimulation using S-wave splitting data: Geophysical Prospecting, **61**, 461–475, doi: 10.1111/j.1365-2478.2012.01132.x.

Vermeer, G. J. O., 2002, 3-D seismic survey design, SEG Geophysical Reference Series vol. 12, SEG.

Vernik, L., and X. Liu, 1997, Velocity anisotropy in shales: A petrophysical study: Geophysics, **62**, 521–532, doi: 10.1190/1.1444162.

Wang, Z., 2002, Seismic anisotropy in sedimentary rocks — Part 2: Laboratory data: Geophysics, **67**, 1423–1440, doi: 10.1190/1.1512743.

Worthington, M. H., 2007, The compliance of macrofractures: The Leading Edge, **26**, 1118–1122, doi: 10.1190/1.2780780.

Worthington, M. H., and J. A. Hudson, 2000, Fault properties from seismic *Q*: Geophysical Journal International, **143**, 937–944, doi: 10.1046/j.1365-246X.2000.00315.x.

Xia, G., L. Thomsen, and O. Barkved, 2007, Fracture detection from seismic P-wave azimuthal AVO analysis — Application to Valhall LoFS data, *in* M. Lu, C. C. Li, H. Kjorholt, and H. Dahle, eds., In-situ rock stress: Taylor & Francis, 521–529.

Jon Downton received a B.S. (1985) in geophysics from the University of Alberta and a Ph.D. (2005) from the University of Calgary. He is a senior research advisor for CGG GeoSoftware. He has worked as a reservoir geophysicist, research geophysicist, and research manager. His work focuses on reservoir geophysics and the seismic processing associated with it. His current research is the prediction of fractures and stress from seismic anisotropy. He has extensive experience in estimating rock and fluid properties from seismic data, including AVO, inversion, and rock physics. He has presented numerous papers at SEG, EAGE, and CSEG conferences, for which he has received best paper awards. He has also been a keynote speaker at ASEG, CSEG, and EAGE conferences. He is a member of CSEG, SEG, EAGE, and APEGA and is a past president of the CSEG.

Benjamin Roure is a senior geophysical researcher with CGG, with 10 years of experience in the seismic reservoir characterization research and development group. His main interest is inversion algorithms (3D, 4D, azimuthal, multicomponent). He has published and presented papers at various conferences including SEG, EAGE, and CSEG. With his coauthors, he received the best *Recorder* paper award from CSEG in 2011.